The Astrophysical Journal, 799:60 (21pp), 2015 January 20 doi:10.1088/0004-637X/799/1/60

BRIGHTEST X-RAY CLUSTERS OF GALAXIES IN THE CFHTLS WIDE FIELDS: CATALOG AND OPTICAL MASS ESTIMATOR

M. Mirkazemi[1], A. Finoguenov[1,2,3], M. J. Pereira[4], M. Tanaka[5], M. Lerchster[1], F. Brimioulle[6], E. Egami[4], K. Kettula[2,12], G. Erfanianfar[1], H. J. McCracken[7], Y. Mellier[7], J. P. Kneib[8], E. Rykoff[9], S. Seitz[1,6], T. Erben[10], and J. E. Taylor[11]

[1] Max-Planck-Institut für extraterrestrische Physik, Giessenbachstraße, D-85740 Garching, Germany; kazemi@mpe.mpg.de
[2] Department of Physics, University of Helsinki, Gustaf Hällströmin katu 2a, FI-00014 Helsinki, Finland
[3] University of Maryland Baltimore County, 1000 Hilltop Circle, Baltimore, MD 21250, USA
[4] Steward Observatory, University of Arizona, 933 North Cherry Avenue, Tucson, AZ 85721, USA
[5] National Astronomical Observatory of Japan, 2-21-1 Osawa, Mitaka, Tokyo 181-8588, Japan
[6] Universitätssternwarte München, Scheinerstrasse 1, D-81679 München, Germany
[7] Institut d'Astrophysique de Paris, UMR7095 CNRS, Université Pierre et Marie Curie, 98 bis Boulevard Arago, F-75014 Paris, France
[8] Laboratoire d'Astrophysique de Marseille, CNRS-Université, Ple de l'Etoile Site de Château-Gombert 38, rue Frédéric Joliot-Curie, F-13388 Marseille Cedex 13, France
[9] SLAC National Accelerator Laboratory, Menlo Park, CA 94025, USA
[10] Argelander Institute for Astronomy, University of Bonn, Auf dem Hügel 71, D-53121 Bonn, Germany
[11] Department of Physics and Astronomy, University of Waterloo, 200 University Avenue West, Waterloo, ON N2L 3G1, Canada
[12] Helsinki Institute of Physics, P.O. Box 64, FI-00014 University of Helsinki, Finland
Received 2014 March 23; accepted 2014 November 11; published 2015 January 15

ABSTRACT

The Canada–France–Hawaii Telescope Legacy Survey (CFHTLS) presents a unique data set for weak-lensing studies, having high-quality imaging and deep multiband photometry. We have initiated an *XMM*-CFHTLS project to provide X-ray observations of the brightest X-ray-selected clusters within the wide CFHTLS area. Performance of these observations and the high quality of CFHTLS data allow us to revisit the identification of X-ray sources, introducing automated reproducible algorithms, based on the multicolor red sequence finder. We have also introduced a new optical mass proxy. We provide the calibration of the red sequence observed in the Canada–France–Hawaii filters and compare the results with the traditional single-color red sequence and photo-z. We test the identification algorithm on the subset of highly significant *XMM* clusters and identify 100% of the sample. We find that the integrated z-band luminosity of the red sequence galaxies correlates well with the X-ray luminosity, with a surprisingly small scatter of 0.20 dex. We further use the multicolor red sequence to reduce spurious detections in the full *XMM* and *ROSAT* All-Sky Survey (RASS) data sets, resulting in catalogs of 196 and 32 clusters, respectively. We made spectroscopic follow-up observations of some of these systems with HECTOSPEC and in combination with BOSS DR9 data. We also describe the modifications needed to the source detection algorithm in order to maintain high purity of extended sources in the shallow X-ray data. We also present the scaling relation between X-ray luminosity and velocity dispersion.

Key words: catalogs – cosmology: observations – galaxies: clusters: general – surveys – X-rays: galaxies: clusters

Supporting material: machine-readable tables

1. INTRODUCTION

In the past two decades the accelerating expansion of the universe has been confirmed by several experiments, such as observations of supernovae (e.g., Riess et al. 1998; Perlmutter et al. 1999) and measurements of the cosmic microwave background (CMB; e.g., Spergel et al. 2003). This acceleration is thought to be a consequence of dark energy density, which, in the simplest way, can be modeled by a nonzero Einstein cosmological constant. Understanding the origin of the associated phenomenon of dark energy is among the most important tasks for understanding the formation and evolution of the universe. Galaxy clusters play an important role in this through their sensitivity to the growth of structure. One of the first efforts in constraining cosmology with galaxy clusters was made by Borgani et al. (2001). They measured Ω_M using 103 galaxy clusters in the *ROSAT* Deep Cluster Survey (RDCS; Rosati et al. 1998) out to $z \simeq 0.85$. In the subsequent study, Vikhlinin et al. (2009) obtained updated measurements of $\Omega_M h$, as well as the dark energy equation of state, ω_0, and the amplitude of power spectrum, σ_8. For a review of cosmological constraints obtained using galaxy clusters in the past decade, see Weinberg et al. (2013) and Allen et al. (2011). The 2013 *Planck* results have revealed a tension between a combination of CMB TT fluctuation spectrum and baryonic acoustic oscillation measurements versus galaxy cluster abundance (Planck Collaboration et al. 2014). The physical interpretation of the results in view of the nonzero neutrino mass requires a robust understanding of the cluster scaling relations.

From an astrophysical point of view, X-ray cluster survey data provide an important definition of high-density environment, critical for studies of galaxy formation (e.g., Tanaka et al. 2008; Giodini et al. 2009; Balogh et al. 2011; Giodini et al. 2012) and active galactic nuclei (AGNs; e.g., Silverman et al. 2009, Tanaka et al. 2012, Allevato et al. 2012).

The main aim of this paper is to address the cluster identification using Canada–France–Hawaii Telescope Legacy Survey (CFHTLS) data and to provide the cluster sample and scaling relations between optical and X-ray luminosity. The calibration between weak-lensing mass and X-ray observables (luminosity and temperature) will be presented in Kettula et al. (2014).

Optical galaxy cluster searches are often hindered by galaxy projection effects. Several algorithms have been applied to solve this problem. In addition to employing photometric methods such as red sequence identification (Gladders & Yee 2000) and MaxBCG (Annis et al. 1999; Koester et al. 2007), the detection of extended X-ray sources is often a reliable indication of galaxy clusters (Rosati et al. 2002). With the increased number of X-ray surveys in the past decade, such as Chandra Deep Field North (Bauer et al. 2002), Chandra Deep Field South (Giacconi et al. 2002), Lockman Hole (Finoguenov et al. 2005), Cosmic Evolution Survey (COSMOS; Finoguenov et al. 2007), *XMM*-Large Scale Structure (*XMM*-LSS; Pacaud et al. 2007), Canadian Network for Observational Cosmology (Finoguenov et al. 2009), and Subaru-*XMM* Deep Field (Finoguenov et al. 2010), X-ray astronomy has introduced itself as an efficient cluster and group detection tool. In addition, X-ray properties of clusters can be used to best characterize the cluster mass, a requirement for precision cosmology work (Kravtsov et al. 2006; Nagai et al. 2007).

In this paper we explore the use of multiwavelength data to identify X-ray clusters within the *ROSAT* All-Sky Survey (RASS) data. RASS data are both faint and unresolved, so cluster confirmation is challenging. In order to establish a reliable method, we used the highly significant extended sources, obtained through our *XMM-Newton* follow-up program. We start with a description of the *XMM* data reduction and detection of extended sources in Section 2. In Section 3 we present the cluster identification and validation, including spectroscopic follow-up program and velocity dispersion measurements for a subsample of clusters. Section 4 provides the X-ray cluster catalogs for both *XMM* and RASS and compares the optical luminosity and X-ray luminosity of clusters. In Section 5 we summarize and discuss the results. Throughout this paper we use the AB magnitude system and consider a cosmological model with $H_0 = 72$ km s^{-1} Mpc^{-1}, $\Omega_\Lambda = 0.75$, and $\Omega_M = 0.25$.

2. DATA

2.1. X-Ray Data

The main aim of the *XMM*-CFHTLS program is to efficiently find massive galaxy clusters, through a series of short *XMM-Newton* follow-up observations of faint RASS sources (Voges et al. 1999) identified as galaxy clusters using CFHTLS imaging data. In total, 73 observations of cluster candidates have been performed, using 220 ks of allocated time. At the time of scheduling *XMM* observations, only T0005 CFHTLS data have been publicly released, which covered 100 deg^2 in partial W1 and W4 fields and the full W2 field. In order to use the mosaicking mode of *XMM-Newton*, we had to fulfill the repointing constraint of 1°. Given the low density of RASS sources, the number of robust clusters was rather low, and for *XMM* snapshot observations, we also pointed to the RASS sources identified with a photo-z galaxy overdensity. Performance of this program has allowed us both to select the adequate method for cluster identification and to perform extensive *XMM* studies of optically selected clusters.

The current RASS catalogs include 122 deg^2 (in W1, W2, and W4), while we only have observed with *XMM* the clusters selected from ∼90 deg^2 (in W2, W4, and half of W1). We would like to advise against using our data for studying the cluster abundance, as our program selectively points to clusters selected from 90 deg^2, while covering 14 deg^2. Use of our catalogs for cluster abundance studies would need to both account for RASS sensitivity and only use our RASS source list, while some of the bright *XMM* sources were filler optical clusters to ensure repointing constraints.

In our final catalog, we also include existing serendipitous observations, since some candidate clusters have already been previously observed with *XMM*. We exclude from our survey the *XMM*-LSS (and XXL) fields, where clusters are identified by the corresponding teams (e.g., Pacaud et al. 2007). We direct interested readers to Gozaliasl et al. (2014), where we present our catalog using the 3 deg^2 overlap between the XMM-LSS survey and CFHTLS.

Our survey methodology is to cover a large area of the sky with short X-ray exposures. The detection of sources in such a shallow survey explores the Poisson regime, so there is a need for tailored data reduction methods. Confirming RASS sources does not require any sophisticated modeling, given that they are typically $>20\sigma$ sources, but detection of fainter serendipitous sources requires a new approach.

The procedure of Finoguenov et al. (2007, 2009), with updates described in Bielby et al. (2010), has been further revised to store the locally estimated background and exposure maps separately in order to treat the Poisson noise within the source detection program (wvdetect; Vikhlinin et al. 1998). Furthermore, we modified the ratio of thresholds for point and extended sources, setting the detection of point sources to 3.3σ and that of extended sources to 4.6σ. This choice of thresholds prevents detection of point sources only on large spatial scales. The consideration of the detection effect is very general, but the ratio of thresholds is tailored for the *XMM* point-spread function (PSF) and the scales of source detection we employ. In detecting the extended source, we avoid detecting the point sources, by detecting them on small scales and subtracting their flux according to PSF model, so no detection occurs on any scale anymore. The terms small and large scales are specific to *XMM* and refer to scales below and above 16″, respectively. If the source is not detected on small scales, but only detected on large scales, it would be mistaken for an extended source. An example of such a detection is a source with 3 counts in the central 16″radius and 2 more counts beyond this radius. For *XMM-Newton*, the PSF model predicts 40% of the point-source flux to occur on the scales we use for the extended source detection. The odds of not detecting the central 60% of the point-source flux while detecting 100% of the source flux by including the outskirts are large, especially if only a few counts suffice for a detection. To beat this contamination down, we need to increase the threshold for detecting the large scales, so that the odds of detecting the outer 40% of the flux with a new large threshold and not detecting the central flux of the source with the original threshold are small, where small is set to be 1%, since this makes a 10% contamination to extended sources, given that point sources are 10 times more abundant. We also decrease the threshold for detecting the flux on small scales. Given the PSF shape of *XMM*, we find the suitable detection limits to be 3.3σ for the central flux and 4.6σ for the outskirts. We also require the significance of the flux determination associated with the detection to be above 4.6σ. The problem described above is typical to shallow surveys and, for example, will be important for eROSITA (Predehl et al. 2010). In deep surveys, extended source detection is background limited, which requires more counts for large scales to be detected at similar thresholds, and so the flux on small scales is always detected from a point source.

The 4.6σ threshold *XMM* source list is expected to have less than 10% contamination of point sources to the extended source catalogs, which we consider acceptable, given that the

highest identification rate for extended sources in deep fields is 90% (e.g., Finoguenov et al. 2010). The corresponding chance identification rate is expected to be below 2%. These estimates are conservative, since all sources in this list were identified. As in our previous work, while removing flux from point sources, we are not going through the step of cataloguing the sources, as we model the point-source contamination by convolving the wavelet images on small scales with a kernel reproducing the PSF shape on large scales.

For the provisional catalog of sources found at lower X-ray σ (<4.6), the contamination from point sources increases to 50%. The final rate for spurious identification for such source selection is reduced owing to sparse density of matching sources (optical clusters) and amounts to 10%. Given the high expected level of chance identification, this catalog is not included in the analysis of scaling relation between X-ray luminosity and integrated optical luminosity.

2.2. Optical, Photometric Redshift and Spectroscopic Data

During 2003–2009, the 3.6 m Canada–France–Hawaii Telescope (CFHT) completed a very large imaging program known as the CFHTLS using the 2048 × 4612 pixel wide-field optical imaging camera MegaCam. With a 0.″185 pixel size, CFHT MegaCam gives a 0.°96 × 0.°96 field of view. All the observations were done in dark and gray telescope time (∼2300 hr). Four wide fields of this survey, with a total area amounting to 170 deg^2, were observed in u^*, g', r', i', and z' band down to i'= 24.5. In this work, we use the T0007[13] data release of CFHTLS and corresponding photometric redshift catalog.[14] The photometric redshifts were computed in a similar manner to the methods of Ilbert et al. (2006) and Coupon et al. (2009). The photometric redshift catalog is limited to $i' = 24$, and according to the report of the CFHTLS team, the achieved photometric redshift accuracy and outlier rates are $\sigma_{\Delta z\backslash 1+z} \cong 0.07$ and $\eta \cong 13\%$ for galaxies with $22.5 \leqslant i' \leqslant 23.5$ (almost the faintest galaxies in this survey). We use optical data from three wide fields of CFHTLS: W1, W2, and W4.

Follow-up observations of clusters in W1, W2, and W4 fields were performed using Hectospec on MMT. Hectospec is a 300 fiber multiobject spectrograph with a circular field of view of 1° in diameter (Fabricant et al. 2005). We used the 270 line grating, which provides a wide wavelength range (3650–9200 Å) at 6.2 Å resolution. We reduced the spectra and measured redshifts using the HSRED pipeline (Cool et al. 2005). Redshifts were determined by comparing the reduced spectra with stellar, galaxy, and quasar template spectra and choosing the template and redshift that minimize the χ^2 between model and data. We then visually inspected the template fits and assigned quality flags based on the certainty of the redshift estimate.

Targets for spectroscopic follow-up were culled from the list of candidates in the *XMM*-CFHTLS fields and prioritized based on a combination of their X-ray flux and photometric redshift. High-priority clusters (with X-ray flux $>7\times10^{-14}$ erg cm^{-2} s^{-1} and $0.15 < z < 0.6$) dictated the locations of the Hectospec pointings; fainter clusters or clusters beyond these redshift limits were used as fillers and therefore only observed if they lay within 30′ of a high-priority target. AGN candidates based on the *XMM*-CFHTLS point-source catalogs were also used as low-priority fillers. The cluster follow-up strategy used varied according to the certainty in the red sequence redshift estimate. For clusters with reliable redshifts, i.e., with a high number of red sequence galaxies, we use photometric redshift catalogs to select only galaxies that lie in the photo-z slice ($dz < n \times (1+z) \times \sigma_{\rm photoz}$, where $\sigma_{\rm photoz}$ is the photometric redshift error and n is an integer number between 2 and 4). The red sequence significance, α, is a parameter that shows the overdensity of galaxies in comparison to the number of background galaxies at the cluster redshift. This parameter will be defined more accurately in Section 3.1. This narrower target selection means we were able to explore the infall regions of the clusters out to larger radii. For clusters with few photo-z counterparts, we performed a magnitude-limited survey at smaller radial distances, with the goal of identifying the optical counterparts and securing a redshift for the X-ray emission. Over the three fields, 32 fiber configurations were observed, mainly in W1 and W2, and secure redshifts for 6170 objects were measured.

In performing the analysis, we have also added spectroscopic data in W1, W2, and W3 from the Sloan Digital Sky Survey III (SDSS-III; Aihara et al. 2011). In total, we have 13 K, 3.5 K, and 9 K spectroscopic redshifts in W1, W2, and W4, respectively.

3. OPTICAL COUNTERPARTS FOR X-RAY SOURCES

3.1. Red Sequence Method

The red sequence (Baum 1959; Bower et al. 1992; Gladders & Yee 2000) is a term defining the overdensity of early-type cluster galaxies in color–magnitude space. Usually a single color is used to find overdensities of early-type galaxies (ETGs) in a limited range of redshifts. This color is selected so that the 4000 Å break is located in the bluer filter. For example, Rykoff et al. (2012) used $g' - r'$ for a redshift range between 0.1 and 0.3. However, if we select another color, such as $r' - i'$ for redshifts below 0.3, ETGs in a cluster still produce a sequence since they have similar formation redshifts and a mostly passive evolution. While background and foreground galaxies (e.g., a late-type galaxy at higher redshift) can have similar color to the color of member ETGs, one can exclude them using other filters. This approach leads to finding member ETGs with less contamination and higher purity in selection of member galaxies, as well as higher sensitivity for cluster detection. On the other hand, multicolor selection of red sequence galaxies may miss some of the red sequence galaxies (lower completeness). Combination of photometric redshift and red sequence selection can also work similarly. In this paper we apply the multicolor selection of red sequence galaxies to find the clusters. We compare the relation between X-ray luminosity and integrated optical luminosity of clusters using three methods: (1) single-color red sequence, (2) multicolor red sequence, and (3) a combination of photo-z and single-color red sequence (regardless of purity and completeness for each method), to know which of them gives a better optical proxy for X-ray luminosity (or mass) of clusters.

The photometric redshifts are available in the T0007 public catalog; thus, we only need to calibrate the red sequence method for the CFHTLS wide survey. In the red sequence method, a model for describing the color of galaxies and its corresponding dispersion as a function of redshift is assumed. Then, at each redshift step, the number of red galaxies with absolute magnitude lower than a threshold is counted (using the model-predicted color value and its dispersion) and corrected for the number of background red galaxies at the same redshift. We denote the mentioned threshold on absolute magnitude

[13] http://terapix.iap.fr/cplt/T0007/doc/T0007-doc.pdf
[14] http://terapix.iap.fr/rubrique.php?id_rubrique=267

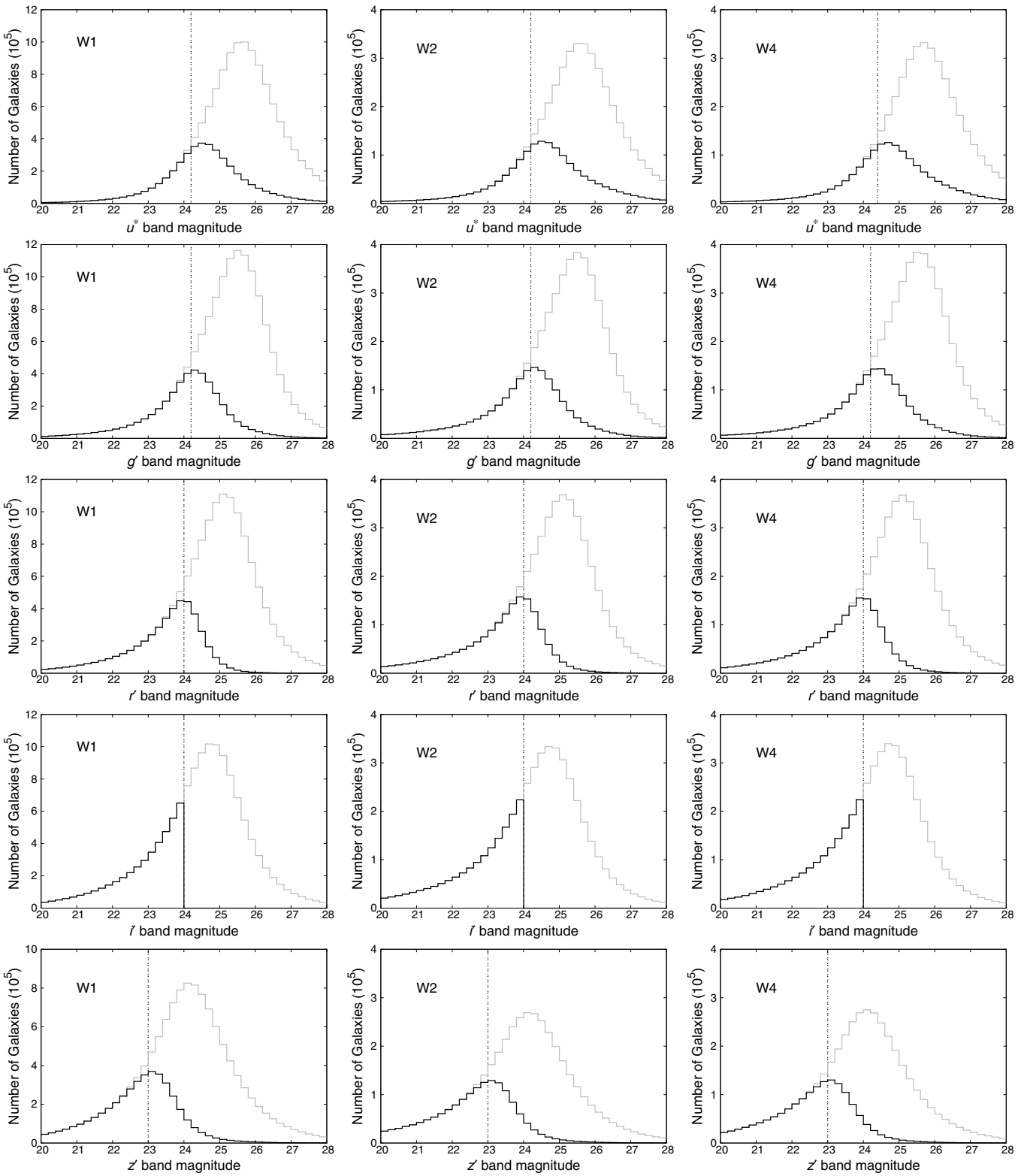

Figure 1. Distribution of the u^*, g', r', i', and z' magnitudes in W1 (solid line), W2 (dashed line), and W4 (dotted line) fields. The gray and black histograms belong to photometry and photometric redshift catalogs. A vertical dotted line in each plot shows the defined completeness threshold magnitude below which the completeness in the photo-z catalog is less than 90%. Since the photometric redshift computed for galaxies is $i' < 24$, the gray and black distributions are identical for galaxies in this range of magnitude.

as $M_{\rm cut}$. It should be adopted according to the depth of the survey in such a way that the completeness is maintained in the whole redshift range. This corrected number is the cluster richness, and the redshift with the highest richness is chosen as the cluster redshift.

As we move to higher redshifts, galaxies more luminous than $M_{\rm cut}$ can still be below the completeness limit of the sample in one or more filters. Figure 1 shows the magnitude distributions of the CFHTLS survey of galaxies in the W1, W2, and W4 fields in photometric catalogs in the five bands. We derived

Table 1
Completeness Magnitude Limits for Each Field

Filter	W1	W2	W4
u^*	24.2	24.2	24.4
g'	24.2	24.2	24.2
r'	24.0	24.0	24.0
i'	24.0	24.0	24.0
z'	23.0	23.0	23.0

Notes. Because the photometric redshift catalog has a cut at $i' < 24$, the completeness thresholds are almost the same for different fields.

Table 2
Maximum Redshift at which Galaxies with Luminosity of 0.2 L_*, 0.4 L_*, and 1.0 L_* have Photometric Redshift in the T0007 Catalog

Filter	0.2 L_*	0.4 L_*	1 L_*
u^*	0.27	0.34	0.42
g'	0.48	0.60	0.71
r'	0.70	0.84	1.05
i'	0.94	1.1	>1.2
z'	1.12	>1.2	>1.2

the photo-z completeness threshold by comparison between the photo-z catalog and photometry catalog. Figure 1 shows magnitude distribution for these two catalogs. We employ a 0.2 mag bin width in calculating the distributions. We defined the completeness in the photo-z catalog as the magnitude above which the photo-z catalog has a completeness below 90%. We display these limits with the dotted vertical lines in Figure 1. Since the photo-z is computed for galaxies brighter than $i' = 24$, the completeness in other filters is almost the same for different fields. Table 1 shows the magnitude completeness limits for each field, derived this way. With the above method, we derive these completeness thresholds for the photo-z catalog: $u^* = 24.2$, $g' = 24.2$, $r' = 24.0$, $i' = 24.0$, and $z' = 23.0$.

For computing any optical quantity at different redshifts, we need to consider an identical cut on rest-frame luminosity for the whole redshift range. The reason is that galaxies with similar absolute magnitude seem fainter at higher redshifts. This cut can also change the scaling relations and their scatters. For example, Rykoff et al. (2012) tested between richness and X-ray luminosity (hereafter L_X) for different L_{cut} from 0.1 L_* to 0.4 L_*, showing that the richness–L_X relation of a cluster sample has the least scatter with $L_{cut} = 0.2\,L_*$. In addition to minimizing the scatter in the richness–L_X relation, we need to check the feasibility of selecting a given value of L_{cut}, given the depths of the survey. Using the Maraston et al. (2009) stellar population model and combining its spectral energy distribution (SED) with CFHT/MegaCam filters, we derive apparent magnitude $m_*(z)$ for all filters and subsequently the k-correction model. $m_*(z)$ is the apparent magnitude of a galaxy with rest-frame luminosity of L_* at a given redshift z. The computation is done by the "Le Phare" package Ilbert et al. (2006). Maraston et al. (2009) showed that their model is in agreement with color evolution of luminous red galaxies in SDSS. This model is based on a single-burst model with a solar metallicity. Similar to Rykoff et al. (2012), we adopt $L_* = 2.25 \times 10^{10}\,L_\odot$.

Figure 2 shows $m_*(z)$ for all five filters derived from our model for redshifts below 1.2. Based on the magnitude completeness of the survey, we estimate the maximum redshift at which a galaxy with luminosity of 0.2, 0.4, and 1 $\times$ L_{cut} can

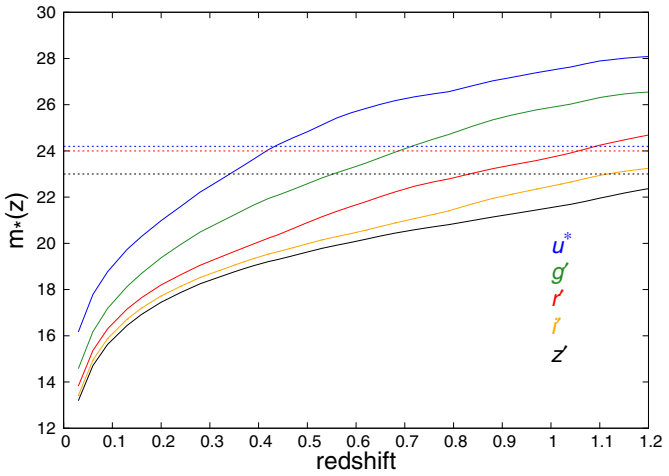

Figure 2. Characteristic magnitude $m_*(z)$ for different filters as a function of redshift. Blue, green, red, yellow, and black solid lines correspond to the magnitudes in u^*, g', r', i', and z' bands, respectively. The blue, red, and black dotted lines show the completeness limits of the survey for u^*/g', r'/i', and z' filters, respectively.

be observed in each filter. Table 2 shows the redshift limits for each M_{cut}.

Given that u^* band is not deep enough to cover at least half of the redshift range of 0.05–1.1, this filter is not used in this work. We chose the following set of redshift ranges, filters, and L_{cut} for the red sequence algorithm:

$0.05 \leqslant z \leqslant 0.6$: $L_{cut} = 0.4\,L_*$ and g',r',i';

$0.6 < z \leqslant 1.1$: $L_{cut} = 0.4\,L_*$ and r',i',z'.

The r'-band detections become incomplete at redshifts beyond 0.84, so the identification there has to rely on a single color. As shown in Figure 2 and Table 2, z' band has the deepest imaging. We have therefore adopted z' band for the magnitude parameter in color–magnitude space. Hereinafter we use m to denote the z' magnitude.

A galaxy is assumed to be on the red sequence at a redshift z if

$$|GC_{a-b} - MC_{a-b}(z)| < 2 \times \sigma_a - b(z), \quad (1)$$

where $a-b$ represents a color ($g'-r'$, etc). GC_{a-b} and $MC_{a-b}(z)$ are galaxy color and model color for red sequence galaxies at redshift z, respectively. $\sigma_a - b(z)$ is the dispersion of the observed galaxy $a-b$ color around the model color. $\sigma_a - b(z)$ is a total dispersion, given by the sum in quadrature of two other parameters, the magnitude errors and the intrinsic width of the color. In the following, we consider these two parameters in detail.

In order to derive the observed color evolution of red sequence galaxies, we use our spectroscopic sample of galaxies at low redshifts and a stellar population model at high redshifts. For low redshift, we select galaxies brighter than $m_*(z)$+1 (or $\leqslant$0.4 L_*) and exclude those with AGN or star-forming classification in spectroscopic data or non-early-type SED, yielding a sample of 7160 ETGs out of the full spectroscopic redshift catalog in W1, W2, and W4. Second, we calculate the average color values and their standard deviation for these galaxies in 16 spectroscopic redshift bins from 0.05 to 0.80 with a bin size of 0.05. For each bin, we discard the galaxies with color offset from the average value exceeding two standard deviations and repeat the calculation of the mean. Figure 3 shows the $g' - r'$, $r' - i'$, and $i' - z'$ colors of ETGs and derived color model as a function of

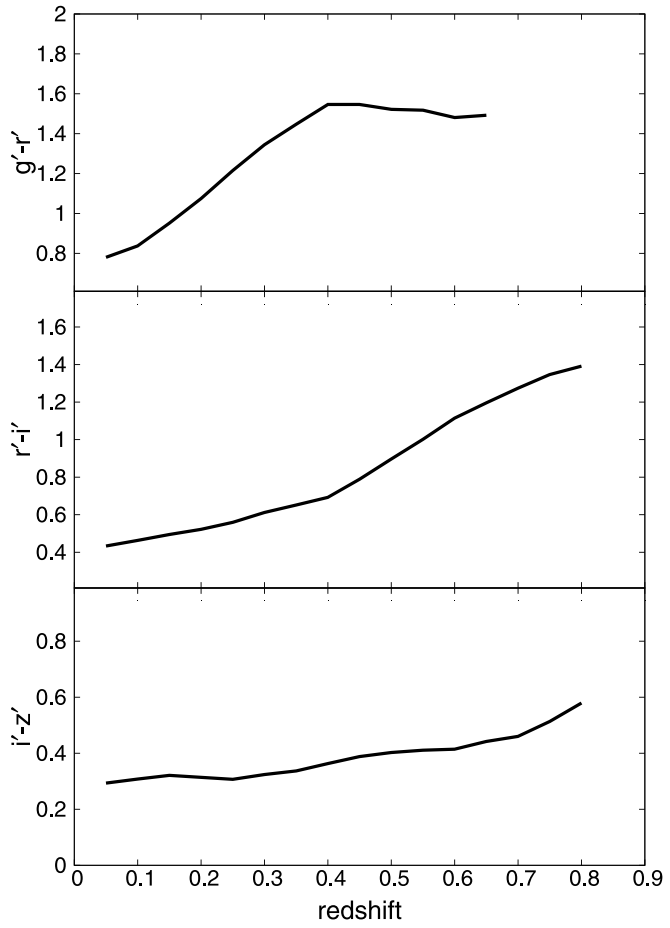

Figure 3. Model colors for ETGs as a function of redshift. Gray dots show the ETGs, and solid lines are the average at each redshift.

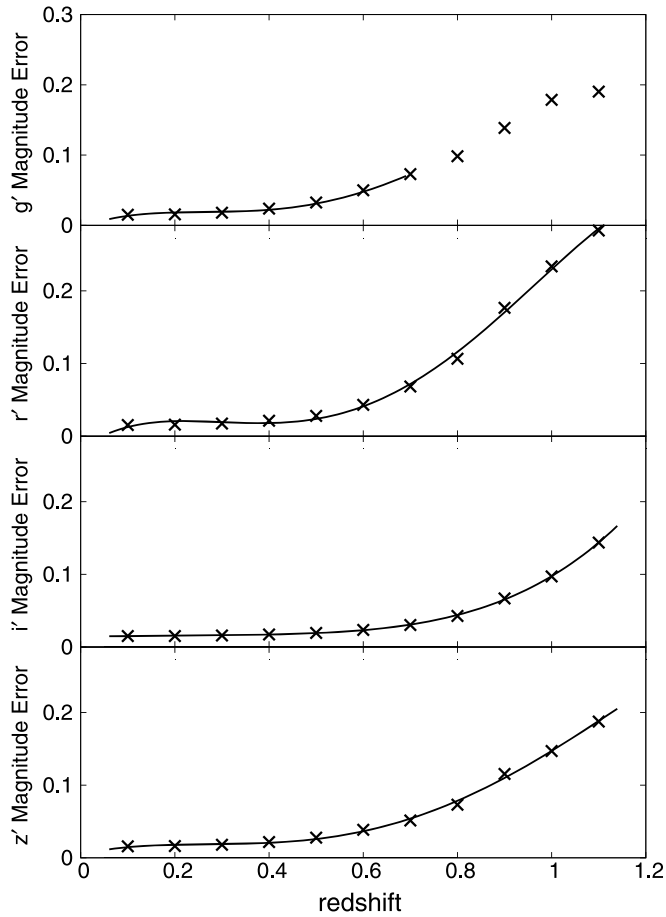

Figure 4. Magnitude errors in g', r', i', and z' band vs. redshift for galaxies brighter than $m_{*(z)}$+1. Crosses show the mean magnitude error for each redshift bin, and solid lines are polynomial fits to the mean values.

redshift (solid lines). Given that the sample of galaxies brighter than 0.4 L_* is incomplete in g band for redshifts above 0.6, the modeling of $g' - r'$ color is limited to z of 0.6.

At higher redshifts, above the redshift of 0.75, the spectroscopic sample of ETGs becomes poor, so we derive $MC_{\rm a-b}(z)$ from the Maraston et al. (2009) model for ETGs, the same model for $m_*(z)$ in Figure 2.

In order to determine the dispersion of the red sequence color, $\sigma_a - b(z)$, we assume that it has two components, an intrinsic dispersion, $\sigma_a - b$, int(z), and a color error, $\sigma_a - b$, color(z). In estimating $\sigma_a - b$, color(z), we selected the galaxies with photometric redshift below 1.2 and brighter than $m_*(z) + 1$ (similar to the original work of Gladders & Yee (2000)). Using the redshift bin width of 0.1, we determine the mean magnitude error for each band and approximate it with the fourth-order polynomials. Figure 4 illustrates the magnitude errors and the polynomial curves as functions of redshift. The total color dispersion is calculated as a sum of the color errors (derived from the magnitudes errors) and the intrinsic color dispersion in quadrature.

The red sequence is known to exhibit a tilt in the color–magnitude space due to the age–metallicity relation (Nelan et al. 2005). Since we work with both low-mass and high-z clusters, where the age–metallicity relation can be different, we prefer to consider the tilt as part of color scatter. We note that a similar approach is adopted in RedMapper (Rykoff et al. 2014). In estimating the intrinsic color dispersion, we assume that the variation of color in cluster ETGs can be modeled by a variation in metallicity. We use PEGASE.2 stellar population/galaxy formation models to estimate the intrinsic color dispersion. For the reference model, a unit solar metallicity is considered (similar to Eisenstein et al. 2001; Rykoff et al. 2012), and we model the evolution of the dispersion by selecting the metallicity that reproduces the observed color scatter for a subsample of well-observed clusters and a high number (>10) of spectroscopic redshifts. We model $r' - i'$ and $i' - z'$ colors between redshifts 0.05 and 1.2 and $g' - r'$ between 0.05 and 0.66. In the Appendix, it is shown that a linear evolution for intrinsic color dispersion of ETGs is a reasonable assumption, especially for $g' - r'$ and $i' - z'$ colors. Thus, the intrinsic color dispersions at redshifts between the two models were derived by interpolating the model points. We check the color–magnitude diagram for the training sample with different $\sigma_a - b$ associated with different $\sigma_a - b$, int and realize that the metallicity of 0.75 solar is appropriate for the second model to enclose the bulk of the red sequence galaxies within two times σ_{a-b}. Figure 5 illustrates color–magnitude diagrams for three clusters at different redshifts with metallicity of 0.75 and 1 for modeling the intrinsic color dispersion. We do not optimize the width of the red sequence for minimizing the contamination or maximizing the number of member galaxies.

The derived intrinsic dispersions of colors as functions of redshift are

$$\sigma'_g - r'_{,\rm int}(z) = 0.029 + 0.044 \times z \qquad (2)$$

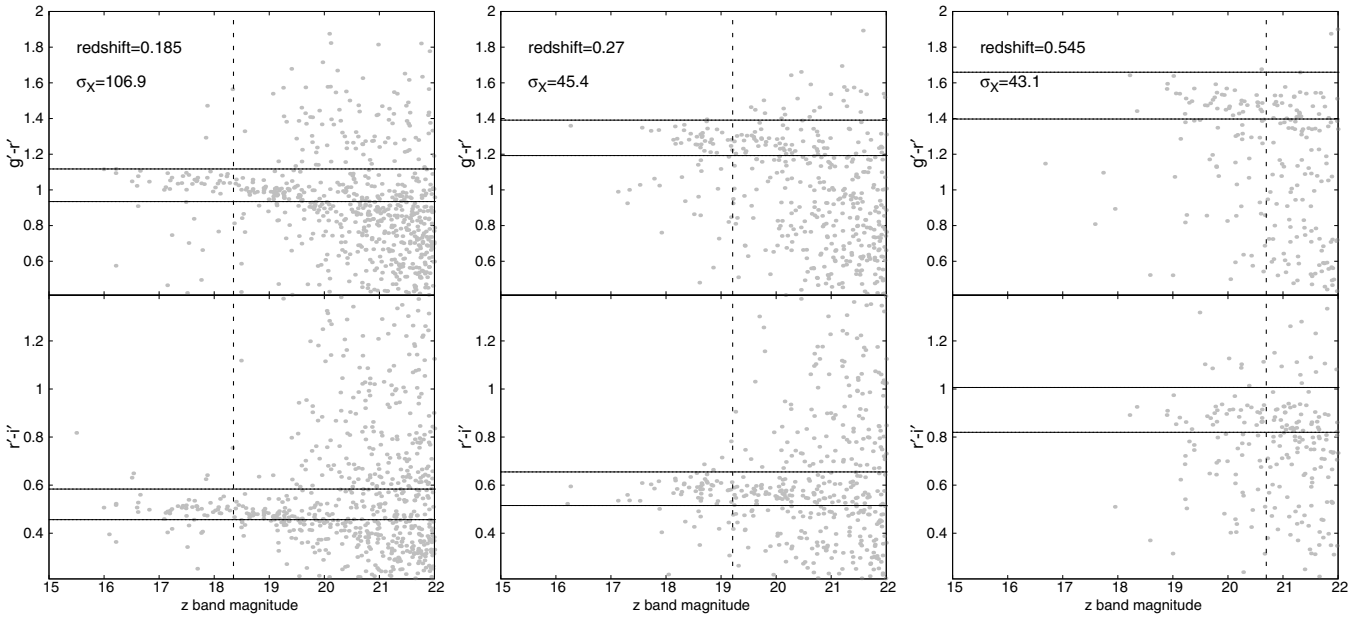

Figure 5. Color–magnitude diagrams for three clusters with a high detection level in X-ray. The solid lines are upper and lower limits on the colors to encompass the bulk of red sequence galaxies. The dashed line is the m_*+1 at the redshift of clusters.

$$\sigma_r' - i'_{,\mathrm{int}}(z) = 0.011 + 0.046 \times z \quad (3)$$

$$\sigma_i' - z'_{,\mathrm{int}}(z) = 0.021 + 0.035 \times z. \quad (4)$$

When running the red sequence finder, we consider a fixed physical radius for galaxy selection and vary the redshift of red sequence from 0.05 to 1.1 with a step of 0.01. At each redshift, we calculate the number of red sequence galaxies brighter than $0.4L_*$, $N_{0.4,R}(z)$. Using 294 random areas in three optical fields, we estimate the background, $\mathrm{NB}_{0.4,R}(z)$, and its standard deviation, $\sigma_{\mathrm{NB}}(z)$. At each redshift we compute the red sequence significance, α, as

$$\alpha = \frac{N_{0.4,\mathrm{R}}(z) - \mathrm{NB}_{0.4,\mathrm{R}}(z)}{\sigma_{\mathrm{NB}}(z)}. \quad (5)$$

The overdensity with the highest red sequence significance is adopted as the X-ray counterpart. The uncertainty in α is estimated by randomly changing the magnitudes of catalog galaxies according to the corresponding photometric errors.

3.2. Applying the Red Sequence Finder to Identify XMM-Newton Extended Sources

We utilize our red sequence finder to identify the counterparts for 133 *XMM-Newton* extended sources in our *primary* sample with a 4.6σ detection limit. We use a galaxy selection radius of 0.5 Mpc, as the centers of *XMM* extended sources correspond well to the cluster center (deviations are less than $15''$; George et al. 2012). Figure 6 illustrates the results of applying the red sequence on a cluster at a redshift of 0.28. After applying the red sequence finder on all the X-ray sources, we visually inspect the correspondence of a two-dimensional distribution of X-ray photons and location of galaxies, presence of secondary peaks in X-rays and optical quality of the images. The photometric and spectroscopic galaxy catalogs are fully utilized during visual inspection for optical counterparts of the X-ray sources. Obvious cluster candidates are marked with a visual flag = 1 in the catalog. Visual flag = 2 is assigned to X-ray sources that have low significance of the optical counterpart or concentration of galaxies almost on the edge or out of the X-ray source, indicative of a confused X-ray source. Figure 7 illustrates clusters with different visual flags. It is worth mentioning that a visual flag (or quality flag) has no utility in this paper; we provide it for others who will use this sample of clusters. We provide an identification to all *XMM* sources with flux significance above 4.6σ. During this inspection, we also visually checked faint sources with detection levels below 4.6, discarding the sources revealing no visual concentration of galaxies. We added 63 clusters from the lower X-ray detection threshold sample, arriving at a sample of 196 clusters with assigned red sequence redshift.

A total of 81 out of 196 clusters have spectroscopic redshift. In defining the spectroscopic redshift, we first visually select the redshift of the brightest galaxy with spectroscopic redshift close to the red sequence redshift of a cluster and assume it as an initial redshift of a cluster. Then we select all galaxies within 0.5 Mpc from X-ray center, and the sigma clipping is done within $\pm 0.005(1 + z)$ around the initial redshift. Finally, the mean of spectroscopic redshifts is computed. The number of spectroscopic counterparts per cluster varies from 1 to 10 member galaxies. In Figure 8 we compare the red sequence redshift with the mean of spectroscopic redshift of member galaxies. The average difference between the red sequence and spectroscopic redshift is 0.002, with a standard deviation of $0.02(1 + z)$.

3.3. Velocity Dispersion

We can also use velocity dispersion measurements as an independent confirmation for the existence of a galaxy cluster and a characteristic for the system. Such a calculation is only reliable for a high number of member galaxies (typically more than 10), though we provisionally calculate dispersions down to systems with five member galaxies and present them in the catalog. We limit the sample for relation between X-ray luminosity and velocity dispersion to the clusters with more

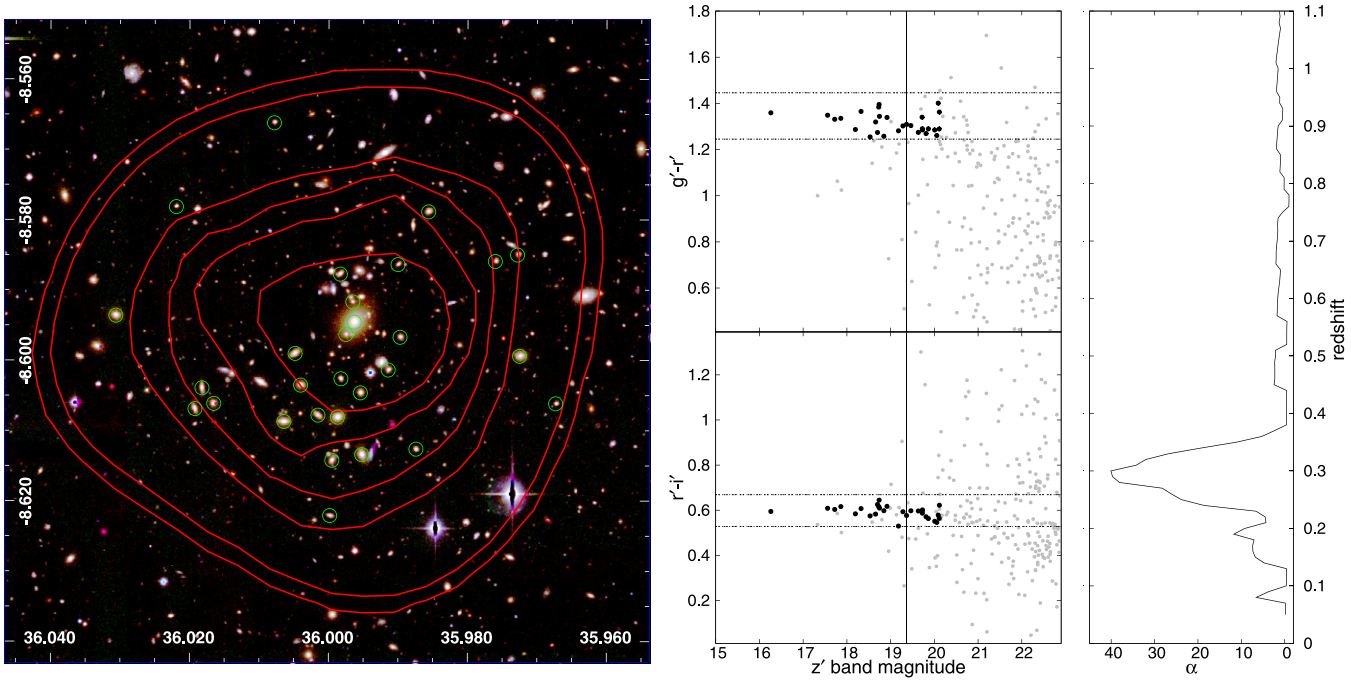

Figure 6. Illustration of the red sequence finder using *XMM* cluster XCC J0224.0-0835 at a red sequence redshift of 0.28. Left: red giant branch (RGB) image of the cluster, where i', r', and g' images are used as red, green, and blue components, respectively. The X-ray flux levels are represented by the red contours, and the green circles are red sequence galaxies brighter than 0.2 L_* within 0.5 Mpc from X-ray center. Middle: color–magnitude diagrams, $g'-r'$ (top) and $r'-i'$ (bottom) vs. z'-band magnitude. Gray points are all galaxies at the redshift of the cluster, located within the radius of 0.5 Mpc from the X-ray source center. Black dots are red galaxies brighter than 0.2 L_* within 0.5 Mpc. In each color–magnitude diagram two horizontal dotted lines are upper and lower limits of color for selecting red galaxies according to an estimate of the color scatter, described in the text. The solid vertical line shows 0.4 L_* at the redshift of 0.3. The middle panels show the corresponding color–magnitude diagrams. The horizontal dashed lines are the lower and upper limits on the color of red sequence galaxies at a redshift of 0.3, and the solid vertical line is $L_{\rm cut} = 0.4\ L_*$ at the same redshift. The gray dots are all the galaxies with projected distances of 0.5 Mpc from the X-ray source center. The black dots are the galaxies with green circles in the left panel. Right: variation of α as a function of redshift with a maximum at redshift of 0.3. The red sequence significance, α, as a function of redshift is shown in the right panel and exhibits a maximum at a redshift of 0.3.

than 10 member galaxies ($N_\sigma \leqslant 10$) because of lower error in velocity dispersion measurement.

We follow the analysis of Connelly et al. (2012). In detail, we select galaxies iteratively, starting with an initial guess for the observed velocity dispersion of $\sigma(z)_{\rm obs}$=500$(1+z)$ km s^{-1} as

$$\delta(z)_{\rm max} = 2\frac{\sigma(z)_{\rm obs}}{c}. \quad (6)$$

We then calculate the spatial distribution associated with $\delta(z)_{\rm max}$:

$$\delta(r)_{\rm max} = \frac{c\delta(z)_{\rm max}}{bh_{71}(z)}, \quad (7)$$

where $b = 9.5$ is the aspect ratio. We use the peak of the X-ray emission as the cluster center. The observed velocity dispersion, $\sigma(z)_{\rm obs}$, is then calculated for galaxies within $\delta(r)_{\rm max}$ using the gapper estimator method (Wilman et al. (2005); Beers et al. (1990)), and the new value is then used to reestimate $\delta(z)_{\rm max}$ and $\delta(r)_{\rm max}$. The procedure is repeated until convergence is achieved. The rest-frame velocity dispersion $\sigma(z)_{\rm rest}$ and intrinsic velocity dispersion $\sigma(z)_{\rm int}$ are finally given by

$$\sigma(v)_{\rm rest} = \frac{\sigma(v)_{\rm obs}}{1+z}, \quad (8)$$

$$\langle\Delta(v)\rangle^2 = \frac{1}{N}\sum_{i=1}^{N}\Delta(v)_i^2, \quad (9)$$

$$\sigma(v)_{\rm intr}^2 = \sigma(v)_{\rm rest}^2 - \langle\Delta(v)\rangle^2, \quad (10)$$

where $\Delta(v)$ is the uncertainty in the spectroscopic velocity measurement. For computing velocity dispersion, we use galaxies with spectroscopic redshift error less than 3×10^{-4}.

The intrinsic velocity dispersion is calculated by subtracting the contribution of redshift errors from the rest-frame velocity dispersion. To assess the velocity dispersion error associated with galaxy sampling, a Jackknife method is applied (Efron 1982), and the associated error is computed as $[N/N-1\sum(\delta_i^2)]^{(1/2)}$, where $\delta_i = \sigma(v)_{\rm obs} - \sigma(v)_{\rm obs,excluding\ \mathit{i}th\ member}$, for a cluster with N member galaxies. Connelly et al. (2012) showed that for calculation of velocity dispersion, applying luminosity-weighted recentering can change the center up to 0.′18 but it does not change the velocity dispersion value. For more detailed description of velocity dispersion calculation, see Connelly et al. (2012) and Erfanianfar et al. (2013, 2014).

To investigate the results of our red sequence finder and velocity dispersion calculation, let us compare $\sigma_{\rm v}$ with $L_{\rm X}$. Figure 9 shows the X-ray luminosity as a function of velocity dispersion for 16 *XMM* clusters with more than 10 spectroscopic counterparts. The black line shows the expected relation between velocity dispersion and X-ray luminosity from Leauthaud et al. (2010). The gray area also shows a 20% error on mass estimate from using the $L_{\rm X}$–$M_{\rm 200c}$ relation (Allevato et al. 2012). We do not account for the intrinsic scatter between velocity dispersion and $M_{\rm 200c}$. The blue and red lines are fitted lines using bisector and orthogonal fitting methods (Akritas & Bershady (1996)). The bisector method minimizes the square distance independently in X and Y directions. The orthogonal method minimizes the squared orthogonal distances. The result of the bisector fitting method is very close to the relation expected

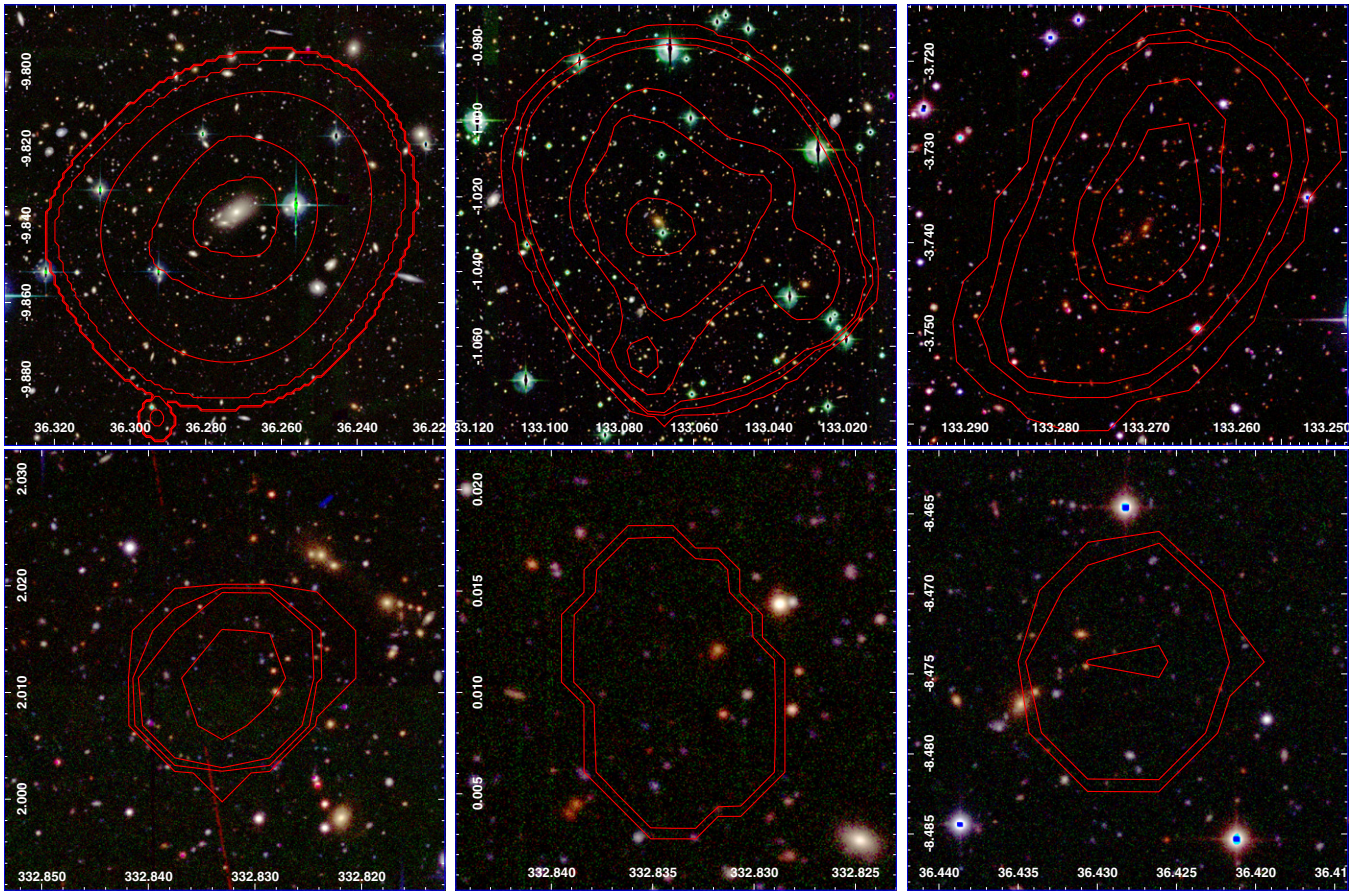

Figure 7. Examples of clusters with different visual flags. Top panels are examples of CFHTLS clusters with visual flag=1 at $z = 0.16$, 0.46, and 0.92 (from left to right), and bottom panels are clusters with visual flag=2 at $z = 0.46$, 0.83, and 0.55 (from left to right). We use the g'-band image as the blue, r' as the green, and i' as the red component of the RGB image. The red contours show the X-ray emission. The upper clusters, from left to right, have X-ray signal significance of 31.03, 43.06, 8.77, and lower ones have 4.51, 2.15, 3.58.

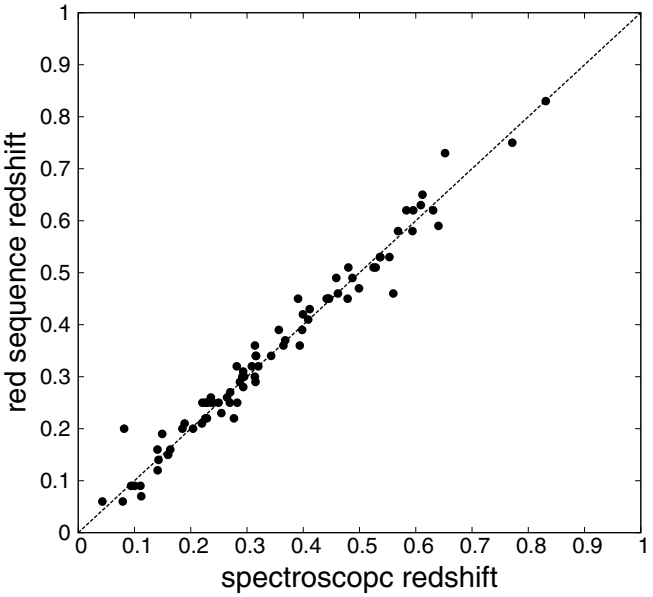

Figure 8. Red sequence redshifts vs. spectroscopic redshifts for 82 clusters with spectroscopic counterparts. The dashed line shows a 1:1 correspondence.

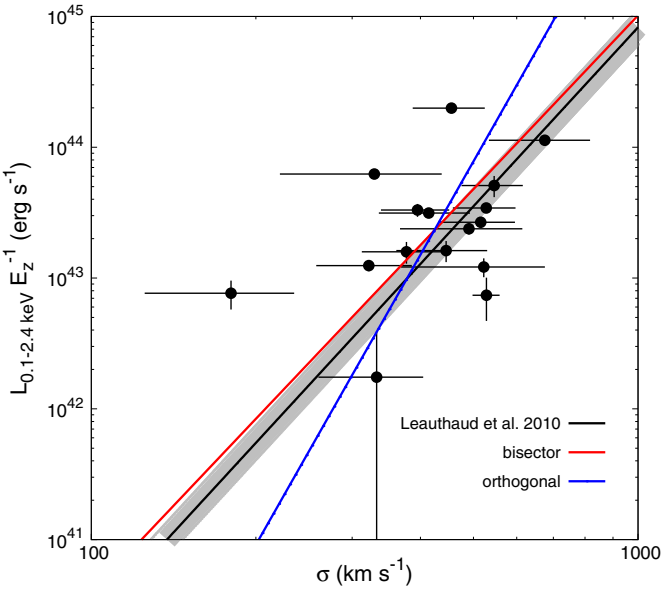

Figure 9. X-ray luminosity vs. the velocity dispersion for *XMM* clusters with more than 10 spectroscopic members from the gapper estimator method. The black line shows expected L_X–σ from the scaling relation. The gray area marks the 20% uncertainty in the mass estimate using the L_X–M_{200c} relation. The red and blue lines are fitted lines with bisector and orthogonal methods. Their equations are $\log(L_X) = (31.77 \pm 4.41) + (5.49 \pm 2.07)\log(\sigma)$ and $\log(L_X) = (24.01 \pm 7.37) + (10.17 \pm 3.84)\log(\sigma)$, respectively.

from the weak-lensing calibration. While most of the clusters are close to the predicted relation, three of them have significantly larger L_X than the values of L_X predicted by the scaling relation. Since this offset is about one order of magnitude in L_X,

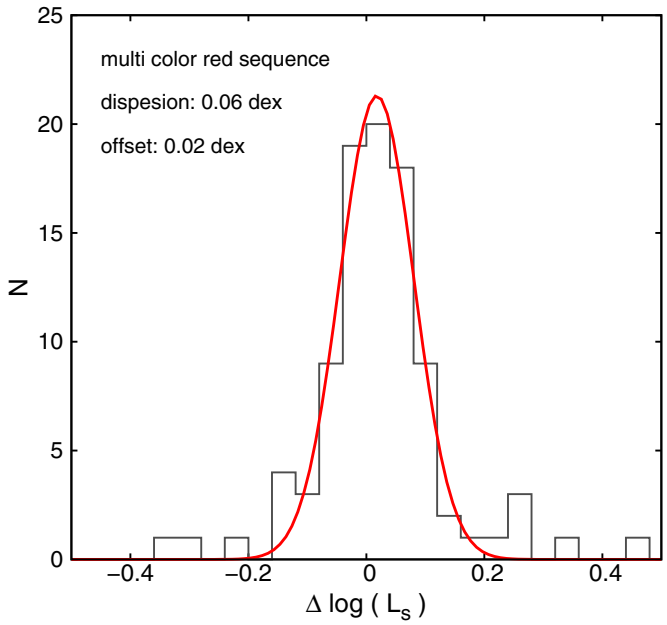

Figure 10. Convergence test for calculating L_S. The plot shows the distribution of L_S calculated within three times $\sigma_{a-b}(z)$ subtracted by the L_S calculated within two times $\sigma_{a-b}(z)$. The distribution is fitted by a Gaussian with a standard deviation of 0.06 dex. The peak offset is 0.02 dex.

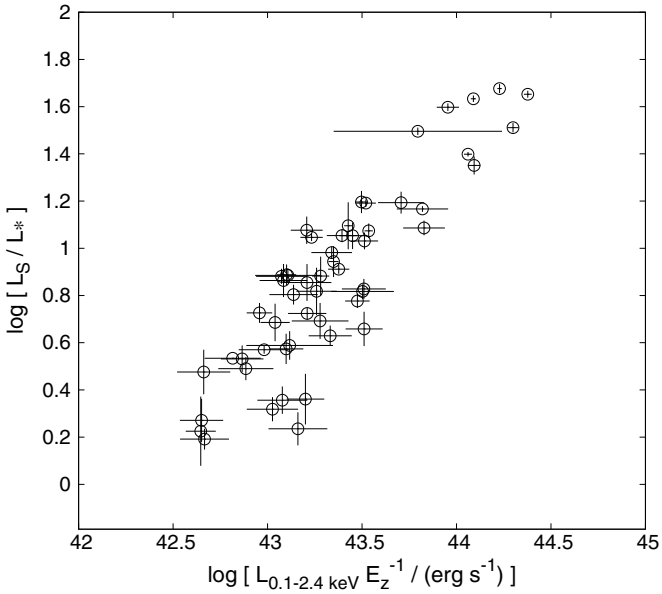

Figure 11. Integrated stellar luminosity in z' band vs. L_X for clusters with X-ray detection level above 4.6 and $0.1 < z < 0.6$.

a significant contribution of unresolved X-ray point sources can be ruled out. Among these three clusters, two less luminous ones have N_σ of 12 and 13, and the more luminous one has 20. As discussed in Ruel et al. (2014), the low number of spectroscopic members can be a reason for these deviations. The compatibility between our σ_v–L_X relation and the scaling relation of Leauthaud et al. (2010) indicates that although the Leauthaud et al. (2010) relation was derived using a sample of clusters mostly with $L_X < 10^{43}$ erg s^{-1}, it is still reliable for mass estimation of more luminous clusters.

3.4. Stellar Luminosity as an L_X Estimator

We calculate the integrated z'-band luminosity, L_S, of red sequence galaxies (brighter than 0.4 L_*) within r_{200c}, for clusters in the redshift range of $0.1 < z < 0.6$ and the X-ray detection threshold above 4.6. The r_{200c} is also calculated from M_{200c} (see Section 4). The luminosities of red sequence galaxies are added to each other and subtracted by background luminosity at the same redshift. The background is the mean of integrated luminosity of the red sequence galaxies at random points in the sky and within a similar radius. In Section 3.1 we mentioned that we define the width of the red sequence to enclose the bulk of bright red sequence galaxies. Here we show that the adopted width does not affect the measured stellar luminosity of the clusters. For this purpose, we increase the widths of all colors in the red sequence selection to three times the $\sigma_{a-b}(z)$ (1.5 times the previous width) and recompute the stellar luminosity. The background computation was also repeated for changing the width of the red sequence. Figure 10 illustrates the variation of L_S after increasing the width of the red sequence by 50%. The change in L_S is 0.02 dex, with a standard deviation of 0.06 dex. We conclude that the obtained L_S values have converged.

In some cases, bright stars affect the photometry. We discard the affected clusters from determination of L_X. Figure 11 illustrates the relation between L_S and L_X for the sample of clusters in the redshift range of $0.1 < z < 0.6$ and the X-ray detection threshold above 4.6. There is a strong correlation between $\log(L_S)$ and $\log(L_X)$ for the bulk of the sample. The Spearman test coefficient for this relation is 0.640, with the zero value for the probability of null hypothesis of null correlation between two quantities.

The good relation between L_S and L_X is a motivation for using L_S as an estimator for L_X and, consequently, the cluster mass. For this purpose, besides L_S within r_{200c}, we also measure the L_S within 1 Mpc from the X-ray center. Figure 12 illustrates the relation between L_S and L_X for the sample of clusters. The upper left and upper right panels show the L_S computed within r_{200c} and 1 Mpc, respectively. The latter is useful in situations when the measurement of the virial radius is not possible or noisy. In Figure 12, the lines show the power-law fits to the relation. The procedures of Akritas & Bershady (1996) ordinary least-squares (OLS) and bi-variate correlated errors and intrinsic scatter (BCES) estimators are used to produce the fits. The OLS estimators in L_X direction (OLS($L_X|L_S$)) and L_S direction (OLS($L_S|L_X$)) are shown as black and green solid curves, respectively. The red dashed lines are the results of the BCES orthogonal fitting method, which minimizes the squared orthogonal distances. The parameters of the plotted relations are listed in Table 3.

For comparison with the multicolor red sequence, we compute the L_S with a single-color selection of red sequence galaxies ($g' - r'$ for $0.05 \leqslant z \leqslant 0.4$ and $r' - i'$ for $0.4 < z \leqslant 0.6$). We also compute the L_S with a combination of photometric redshift and single-color selection of red sequence galaxies. In this method, L_S is computed for galaxies that satisfy both conditions of photo-z range and single color. We need to adopt a suitable redshift range for photo-z selection. A suitable redshift range is the sum in quadrature of two redshift errors, uncertainty in measurement of cluster redshift and errors in photometric redshift of galaxies. In Section 3.2 we show that our red sequence technique has an uncertainty of $0.02(1+z)$ in cluster redshift measurement. The accuracy in photometric redshift varies with galaxy magnitude. We assume the worst photo-z accuracy, which belongs to the galaxies with brightness of m_*+1 at redshift 0.6. According to Figure 8, the z-band magnitude of such a galaxy is 21.1.

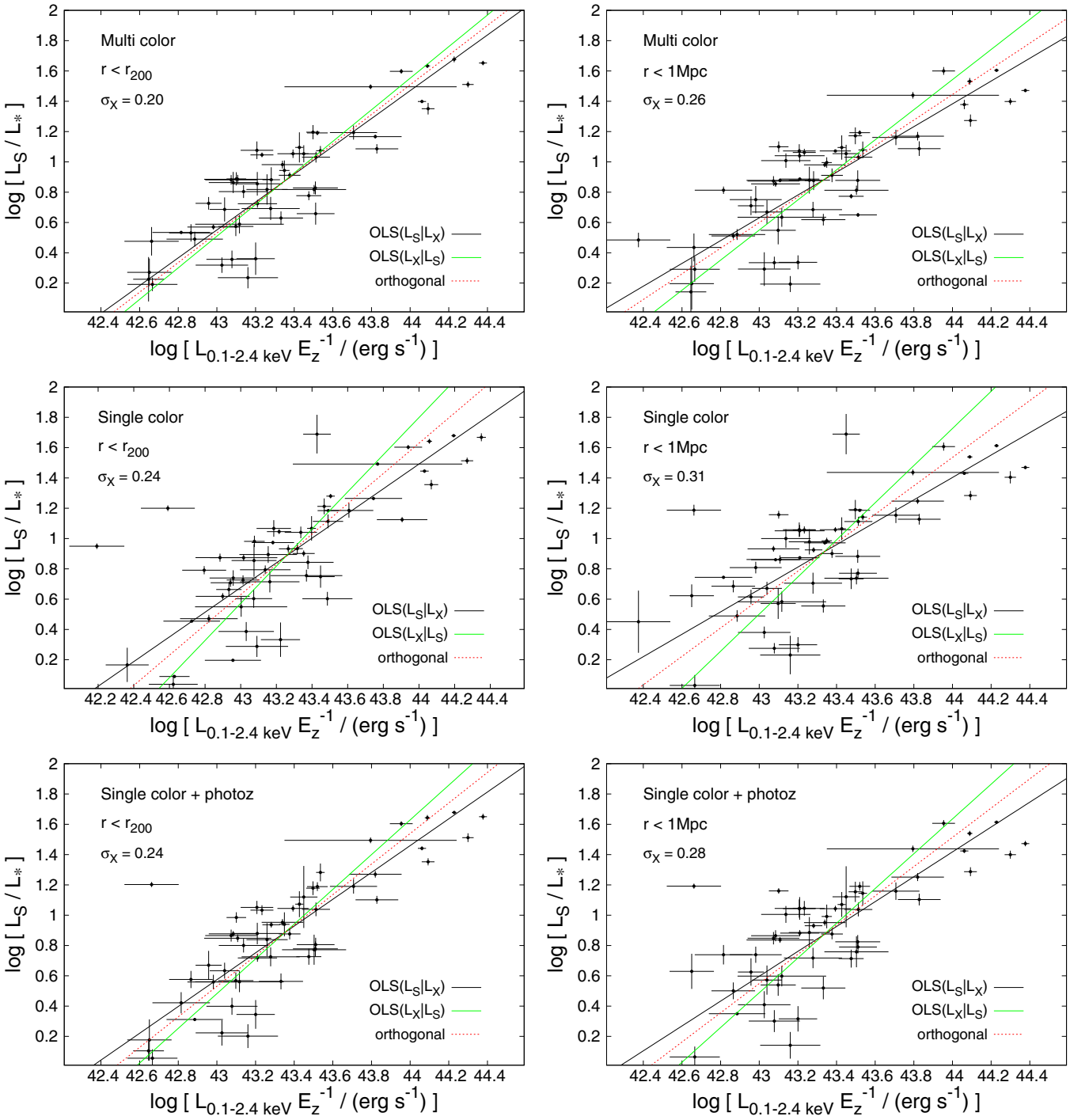

Figure 12. Integrated stellar luminosity in z' band vs. L_X for clusters at $0.1 < z < 0.6$. The right and left panels show the results within r_{200c} and 1 Mpc, respectively. Upper panels use galaxy selection from multicolor red sequence, middle panels are the single-color red sequence, and bottom panels belong to selection by combination of photometric redshift and single-color red sequence. The solid black, solid green, and dashed red lines show OLS($L_S|L_X$), OLS($L_X|L_S$), and orthogonal fits, respectively. In each panel, σ_X is the scatter in L_X direction for the orthogonal fits. The fitting parameters are summarized in Table 3.

We compute the photometric redshift error for galaxies with z-band magnitude between 20.6 and 21.1. For 886 galaxies with such magnitude and with spectroscopic redshift in the three fields of CFHTLS, the photometric redshift error is $0.031(1+z)$. For selection of member galaxies, we adopt the redshift interval of $\pm 0.07(1+z)$ around the mean redshift of the cluster.

The best method (among multicolor, single-color, and single-color-photo-z) is sought to provide the lowest scatter versus L_X. The results are compared in Figure 12, using r_{200c} and 1 Mpc as an extraction radius. The middle and bottom panels of Figure 12 show the relation between the cluster X-ray luminosity and L_S computed using the single-color and single-color-photo-z methods, respectively. These relations are fitted with power-law models, and the results of fitting are shown in Table 3.

For all L_X–L_S scaling relations the scatter for the multicolor red sequence finder is smaller than or equal to the single-color and single-color-photo-z values, independent of the selection radius and the fitting method. For example, for L_S computed

Table 3
Fitting Parameters of $\log(L_X)$–$\log(L_S)$ Relation

Red Sequence	Radius	Fitting	Intercept	Slope	L_X Scatter (dex)	L_S Scatter (dex)
Multicolor	r_{200c}	OLS($L_S|L_X$)	-38.97 ± 2.97	0.92 ± 0.07	0.21	0.19
		OLS($L_X|L_S$)	-44.33 ± 3.21	1.04 ± 0.07	0.20	0.21
		Orthogonal	-41.51 ± 3.11	0.98 ± 0.07	0.20	0.20
Single color	r_{200c}	OLS($L_S|L_X$)	-40.46 ± 5.13	0.95 ± 0.12	0.28	0.27
		OLS($L_X|L_S$)	-54.12 ± 5.39	1.27 ± 0.12	0.25	0.32
		Orthogonal	-47.50 ± 5.03	1.12 ± 0.12	0.26	0.29
Single color + photo-z	r_{200c}	OLS($L_S|L_X$)	-37.47 ± 4.19	0.88 ± 0.10	0.26	0.23
		OLS($L_X|L_S$)	-48.82 ± 4.46	1.15 ± 0.10	0.23	0.27
		Orthogonal	-42.82 ± 3.57	1.01 ± 0.08	0.24	0.24
Multicolor	1 Mpc	OLS($L_S|L_X$)	-31.71 ± 2.95	0.75 ± 0.07	0.28	0.21
		OLS($L_X|L_S$)	-42.15 ± 4.33	0.99 ± 0.10	0.25	0.24
		Orthogonal	-35.77 ± 3.58	0.85 ± 0.08	0.26	0.22
Single color	1 Mpc	OLS($L_S|L_X$)	-31.12 ± 4.35	0.74 ± 0.10	0.37	0.27
		OLS($L_X|L_S$)	-52.18 ± 7.32	1.23 ± 0.17	0.29	0.36
		Orthogonal	-39.75 ± 5.99	0.94 ± 0.14	0.31	0.29
Single color + photo-z	1 Mpc	OLS($L_S|L_X$)	-37.47 ± 4.19	0.88 ± 0.10	0.32	0.26
		OLS($L_X|L_S$)	-48.82 ± 4.46	1.15 ± 0.10	0.27	0.31
		Orthogonal	-42.82 ± 3.57	1.01 ± 0.08	0.28	0.27

Notes. Column 1 indicates the type of selection of red galaxies. Column 2 is the radius within which L_X is calculated. The fitting procedure is listed in Column 3. Columns 4 and 5 present the intercept and slope of fittings, respectively. The scatter in $\log L_X$ and $\log L_S$ direction is given in Columns 6 and 7.

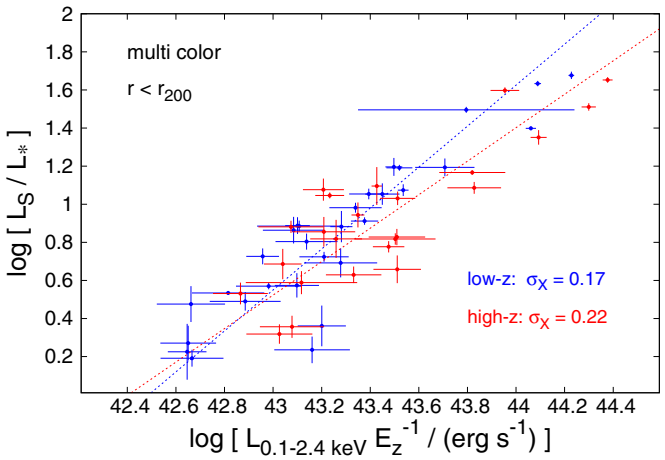

Figure 13. Stellar luminosity vs. X-ray luminosity of clusters for low-redshift (blue dots) and high-redshift (red dots) subsamples. The blue and red lines show the orthogonal fitting results for each subsample, with the parameters presented in Table 3. The fitting parameters are summarized in Table 4.

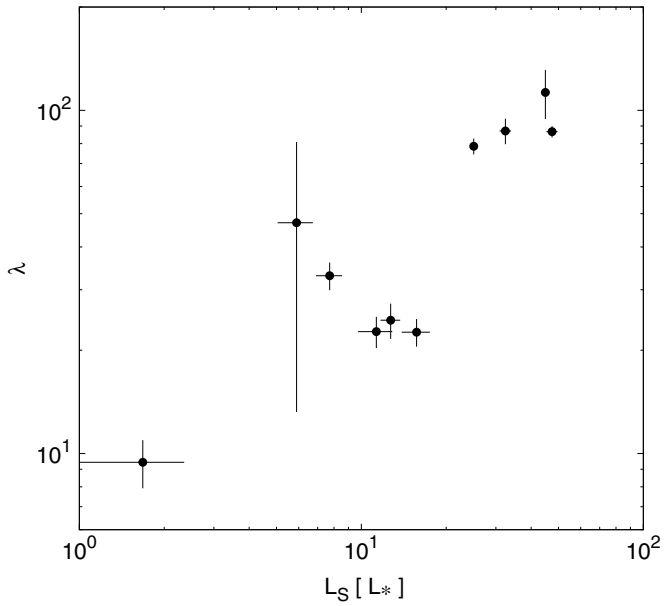

Figure 14. redMaPPer richness parameter λ (calculated using SDSS data) vs. stellar luminosity within r_{200c}, L_S. A good correspondence between two measurements is observed.

with r_{200c}, the orthogonal relation has a scatter of 0.20, 0.29, and 0.24 dex in L_X for multicolor, single color, and a combination of single color and photo-z, respectively. The reduction of scatter is even more significant in the case of a fixed 1 Mpc radius. For instance, the orthogonal scatter is 0.26 dex in L_X for the multicolor, 0.31 dex for the single color, and 0.28 dex for the combination of single color and photo-z. Our results on the tight relation between the L_S and other mass proxies, such as L_X, are in line with the low-redshift studies of Rykoff et al. (2012) at $0.1 < z < 0.3$ and Andreon (2012) for $z < 0.14$.

In Figure 13 we consider the redshift evolution of the L_S–L_X relation. Using two subsamples with $0.1 < z < 0.3$ and $0.3 < z < 0.6$, we find a difference in the relation to X-ray luminosity ($L_X > 42.5\,\mathrm{erg\,s^{-1}}$). The low-redshift relation is within the errors of the high-redshift relation. The parameters of the relation are presented in Table 4. The scatter in L_X reduces down to 0.17 dex for the low-redshift sample.

To compare our red sequence finder to other work, Figure 14 shows L_X versus richness parameter λ used in redMaPPer (next generation of MaxBCG method; Rykoff et al. 2014), designed to find clusters in SDSS data. Briefly, redMaPPer applies a red sequence model and assumes radial and luminosity filters to calculate the probability that a given galaxy belongs to a cluster. The parameter λ is the sum of mentioned probabilities. There are

Table 4
Fitting Parameters of $\log(L_X)$–$\log(L_S)$ Relation for Low- and High-redshift Subsamples

Redshift	Radius	Fitting	Intercept	Slope	L_X Scatter (dex)	L_S Scatter (dex)
$0.1 < z < 0.3$	r_{200c}	OLS($L_S|L_X$)	-44.56 ± 4.10	1.05 ± 0.09	0.17	0.18
		OLS($L_X|L_S$)	-46.69 ± 3.10	1.10 ± 0.09	0.17	0.19
		Orthogonal	-45.69 ± 3.89	1.08 ± 0.09	0.17	0.18
$0.3 < z < 0.6$	r_{200c}	OLS($L_S|L_X$)	-33.61 ± 3.59	0.79 ± 0.08	0.23	0.19
		OLS($L_X|L_S$)	-42.49 ± 5.13	0.10 ± 0.12	0.21	0.21
		Orthogonal	-37.27 ± 4.22	0.88 ± 0.10	0.22	0.19
$0.1 < z < 0.3$	1 Mpc	OLS($L_S|L_X$)	-35.54 ± 3.81	0.84 ± 0.09	0.24	0.21
		OLS($L_X|L_S$)	-43.27 ± 5.65	1.02 ± 0.13	0.23	0.23
		Orthogonal	-38.91 ± 4.38	0.92 ± 0.10	0.23	0.21
$0.3 < z < 0.6$	1 Mpc	OLS($L_S|L_X$)	-29.42 ± 4.14	0.69 ± 0.10	0.29	0.20
		OLS($L_X|L_S$)	-42.79 ± 6.85	1.01 ± 0.16	0.24	0.25
		Orthogonal	-34.25 ± 5.50	0.81 ± 0.13	0.26	0.21

Notes. Stellar luminosity computed using multicolor selection. Column 1 indicates redshift ranges. Column 2 is the radius within which L_X is calculated. The fitting procedure is listed in Column 3. Columns 4 and 5 present the intercept and slope of fittings, respectively. The scatter in $\log L_X$ and $\log L_S$ direction is given in Columns 6 and 7.

10 RASS clusters in overlap between SDSS and the CFHTLS fields. The large errors in λ for a few clusters are caused by the shallow depths of SDSS data. Rozo & Rykoff (2014) reported a scatter of 0.23 dex in X-ray temperature at fixed λ. Figure 14 shows that L_S and λ correlate.

3.5. Applying the Red Sequence Finder to Identify RASS Sources

Performance of our *XMM* program was based on the identification of RASS sources as galaxy clusters. This lead to the development and verification of the source identification methods reported above. It allows us to present a consistent identification of RASS sources using the same method, which allows us to both characterize the target selection and report the clusters that we have not observed, since we include the full CFHTLS data set in this analysis, covering 180 $\deg^2$.

We apply the red sequence finder to identify clusters associated with 245 RASS sources within the three CFHTLS fields in our study. According to the $\log(N)$–$\log(S)$ relation, clusters make up only 10% of X-ray sources (Finoguenov et al. 2007; Cappelluti et al. 2007), making cluster identification difficult using unresolved X-ray sources in RASS data. The radius for galaxy selection has been set to 0.5 Mpc at each redshift, plus 2′to account for the survey PSF of RASS. After finding the red member galaxies, we derive the z'-band luminosity-weighted center for each cluster candidate, which then defines the distance between the optical counterpart and the X-ray source position (hereafter Opt–X-ray distance). Figure 15 shows the red sequence finder results for a cluster at a redshift of 0.19. In order to distinguish between X-ray sources associated with clusters and other X-ray sources, we used Opt–X-ray distance and α parameters. With a comparison between properties of RASS sources and random sources, we try to find X-ray clusters among RASS sources. We similarly apply the red sequence finder on 300 random sources in CFHTLS fields. Figure 16 shows α parameter versus Opt–X-ray and redshift for RASS and random sources. The red circles represent the 245 RASS sources, and black circles are random points in CFHTLS fields. While only a handful of random sources can have high α values (15 or more) and low Opt–X-ray distance, tens of RASS sources achieve such values. This suggests that a combination of α and Opt–X-ray distance can discriminate between clusters and other sources of X-ray emission. We select the X-ray clusters by cuts of $13 < \alpha$ and Opt–X-ray distance less than 2.″5. The left panel in Figure 16 illustrates the cuts with a blue dashed line. Nine random sources and 32 RASS X-ray sources are located in the selection region, which shows the purity (∼80%) in the selected sample of X-ray clusters with this method. We will show in Section 4 that by the adopted criteria we can detect all *XMM* clusters with X-ray flux above the RASS X-ray detection threshold. By increasing the α value, one can achieve a purer sample. For instance, 20 RASS sources have $20 < \alpha$, but only one random source has such a high $20 < \alpha$ value.

4. RASS-CFHTLS AND *XMM*-CFHTLS CATALOGS OF X-RAY-SELECTED CLUSTERS

In this section we present the RASS and *XMM* X-ray-selected cluster catalogs. The first catalog, Table 5, belongs to the 196 *XMM* clusters. The first 133 lines in Table 5 belong to the sample with X-ray detection threshold above 4.6σ, and the last 63 lines are those with a lower detection threshold. Column 1 in Table 5 shows the cluster ID for the *XMM*-CFHTLS sample, with the first digit referring to the CFHTLS wide field (1, 2, or 4). Columns 2 and 3 are, respectively, R.A. and decl. of the X-ray source centers. Columns 4 and 5 are, respectively, the red sequence redshift and red sequence significance, α, of the clusters. Column 6 lists cluster flux and 1 σ error in flux corresponding to the 0.5–2 keV band in units of 10^{-14} erg cm^{-2} s^{-1}. Column 7 reports the rest-frame X-ray luminosity, L_X, in the 0.1–2.4 keV band. The total mass M_{200c}, estimated from the X-ray luminosity using the L_X–M scaling relation and its evolution from Leauthaud et al. (2010), is given in Column 8. Column 9 lists the corresponding radius, r_{200c}, in arcminutes. Spectroscopic redshifts of the clusters are provided in Column 10. For clusters with a spectroscopic redshift in this column, M_{200c} and r_{200c} are computed using spectroscopic redshift. Column 11 reports the visual flag described in Section 3.2. Velocity dispersion and number of spectroscopic members (both described in Section 3.3) for clusters having more than five spectroscopic members are given in Columns 12 and 13, respectively.

The RASS-CFHTLS cluster catalog is listed in Table 6. This catalog includes 32 clusters, with selection shown in the left

Table 5
Catalog of *XMM*-CFHTLS X-ray-selected Galaxy Clusters

ID *XMM*-CFHTLS (1)	R.A. (deg) (2)	Decl. (deg) (3)	R.S. z (4)	α (5)	X-ray Flux 10^{-14} erg cm^{-2} s^{-1} (6)	L_X 10^{42} erg s^{-1} (7)	M_{200c} 10^{13} $M_\odot$ (8)	r_{200c} arcmin (9)	specz (10)	Visual Flag (11)	$\sigma(v)$ (km s^{-1}) (12)	N_σ (13)
XCC J0210.4-0343	32.6184	−3.7202	0.45	0.86 ± 0.92	3.39 ± 0.54	37.08 ± 5.96	14.42 ± 1.44	2.73	0.4417	1	···	1
XCC J0211.0-0905	32.7665	−9.0977	0.45	0.86 ± 1.45	4.28 ± 1.70	48.05 ± 19.15	16.90 ± 4.04	2.838	···	2	···	...
XCC J0211.2-0343	32.8079	−3.7226	0.78	20.48 ± 2.30	7.52 ± 1.04	271.79 ± 37.86	37.77 ± 3.28	2.526	···	1	···	...
XCC J0211.3-0927	32.8338	−9.4567	0.71	1.38 ± 1.17	2.73 ± 1.05	88.06 ± 33.76	19.60 ± 4.52	2.16	···	2	···	...
XCC J0211.4-0920	32.8551	−9.3366	0.84	1.20 ± 0.59	3.83 ± 1.95	173.23 ± 88.38	26.77 ± 8.08	2.148	···	2	···	...
XCC J0211.5-0939	32.8894	−9.6606	0.51	4.82 ± 1.30	3.03 ± 1.41	40.33 ± 18.78	14.70 ± 4.07	2.586	0.4801	2	···	1
XCC J0212.2-0852	33.0716	−8.8752	0.09	1.93 ± 1.72	7.93 ± 3.20	2.62 ± 1.05	3.52 ± 0.85	6.318	0.094	2	···	3
XCC J0213.4-0813	33.37	−8.2204	0.26	2.76 ± 1.02	6.96 ± 1.82	18.04 ± 4.72	10.86 ± 1.74	4.08	0.2358	1	446 ± 84	12
XCC J0213.6-0552	33.4141	−5.8707	1.1	4.40 ± 0.75	2.14 ± 0.91	186.85 ± 80.19	22.11 ± 5.67	1.704	···	2	···	...
XCC J0214.1-0630	33.545	−6.516	0.88	1.03 ± 0.93	1.24 ± 0.47	70.62 ± 26.81	14.52 ± 3.32	1.698	···	2	···	...
XCC J0214.4-0627	33.6064	−6.4605	0.25	13.80 ± 1.26	27.67 ± 49.35	69.48 ± 123.92	25.73 ± 23.81	5.424	0.2366	1	329 ± 108	12
XCC J0215.6-0702	33.9113	−7.0478	1.02	−1.78 ± 0.33	1.33 ± 0.43	104.43 ± 33.88	16.39 ± 3.22	1.614	···	2	···	...
XCC J0215.7-0654	33.9274	−6.9051	0.23	2.76 ± 1.02	5.79 ± 1.48	17.83 ± 4.56	10.62 ± 1.66	3.804	0.2544	1	377 ± 65	10
XCC J0216.1-0935	34.0291	−9.5885	0.62	21.55 ± 1.39	5.95 ± 0.86	121.63 ± 17.66	26.81 ± 2.43	2.706	0.5955	1	···	4
XCC J0216.5-0658	34.1416	−6.9691	1.1	−2.59 ± 0.25	1.26 ± 0.54	118.05 ± 50.52	16.48 ± 4.22	1.542	···	2	···	...
XCC J0216.7-0934	34.1938	−9.5702	0.94	7.82 ± 0.69	1.58 ± 0.51	101.42 ± 33.12	17.31 ± 3.43	1.728	···	2	···	...
XCC J0217.5-0655	34.3779	−6.9236	1.01	0.30 ± 0.34	1.38 ± 0.78	106.01 ± 60.14	16.70 ± 5.56	1.632	···	2	···	...
XCC J0217.5-0936	34.3788	−9.6136	0.39	3.87 ± 1.31	1.70 ± 0.60	14.43 ± 5.15	8.25 ± 1.78	2.49	···	2	···	...
XCC J0217.5-0927	34.3874	−9.462	0.46	5.85 ± 3.15	6.80 ± 2.38	120.11 ± 42.06	27.48 ± 5.82	2.85	0.56	1	···	2
XCC J0217.8-0641	34.4574	−6.689	1.04	−0.03 ± 0.73	2.13 ± 0.99	165.26 ± 76.94	21.59 ± 5.98	1.746	···	2	···	...
XCC J0217.9-0648	34.4871	−6.8068	0.84	−0.79 ± 0.51	1.28 ± 0.51	64.99 ± 26.26	14.29 ± 3.46	1.74	···	2	···	...
XCC J0218.0-0937	34.5029	−9.6256	0.15	1.79 ± 1.07	4.46 ± 0.89	4.75 ± 0.95	4.91 ± 0.61	4.374	0.1598	1	232 ± 73	9
XCC J0218.3-0942	34.5814	−9.7028	0.45	3.86 ± 3.18	2.62 ± 0.73	21.93 ± 6.11	10.78 ± 1.83	2.718	0.3908	1	···	1
XCC J0219.6-0759	34.9039	−7.9882	0.86	1.13 ± 0.94	1.63 ± 0.52	85.26 ± 27.47	16.69 ± 3.26	1.806	···	1	···	...
XCC J0220.1-0836	35.031	−8.6072	0.07	0.97 ± 3.36	16.87 ± 8.29	2.98 ± 1.46	3.90 ± 1.13	8.604	···	2	···	...
XCC J0220.3-0730	35.0849	−7.5027	0.99	−0.47 ± 0.68	3.79 ± 0.89	247.01 ± 58.32	29.23 ± 4.24	1.992	···	2	···	...
XCC J0220.6-0839	35.167	−8.6639	0.07	0.97 ± 2.91	5.16 ± 2.38	2.48 ± 1.14	3.36 ± 0.92	5.292	0.1121	1	410 ± 174	5
XCC J0220.9-0838	35.2279	−8.6402	0.51	6.82 ± 4.29	1.21 ± 0.41	21.01 ± 7.28	9.30 ± 1.95	2.076	0.5251	1	···	1
XCC J0221.2-0846	35.3163	−8.7702	0.09	1.93 ± 1.72	7.00 ± 1.88	2.10 ± 0.56	3.07 ± 0.50	6.282	···	2	···	...
XCC J0221.5-0630	35.3822	−6.515	1.03	3.10 ± 0.31	2.18 ± 1.03	165.18 ± 78.29	21.78 ± 6.13	1.764	···	2	···	...
XCC J0221.5-0830	35.3904	−8.5108	1.07	−0.68 ± 0.41	1.89 ± 0.68	157.79 ± 57.54	20.39 ± 4.49	1.686	···	2	···	...
XCC J0221.6-0618	35.4101	−6.316	0.61	7.58 ± 1.42	2.32 ± 0.74	54.07 ± 17.39	15.74 ± 3.07	2.226	···	2	···	...
XCC J0221.6-0825	35.4113	−8.4271	1.04	−0.03 ± 0.89	1.55 ± 0.55	124.93 ± 44.92	18.05 ± 3.92	1.644	···	2	···	...
XCC J0221.9-0857	35.4915	−8.9622	0.28	2.71 ± 1.88	3.34 ± 0.78	14.36 ± 3.35	8.95 ± 1.28	3.198	0.2933	1	···	4
XCC J0222.8-0623	35.7098	−6.3935	0.39	0.87 ± 1.31	3.16 ± 0.96	26.20 ± 8.01	12.09 ± 2.25	2.826	···	2	···	...
XCC J0223.2-0830	35.8101	−8.514	0.14	1.80 ± 2.08	5.97 ± 1.80	4.75 ± 1.43	4.99 ± 0.91	4.944	···	2	···	...
XCC J0223.8-0826	35.9663	−8.4449	0.71	3.38 ± 1.20	1.08 ± 0.37	38.15 ± 13.11	11.47 ± 2.38	1.806	···	1	···	...
XCC J0223.8-0821	35.967	−8.3552	0.22	8.8 ± 3.06	13.08 ± 2.30	31.25 ± 5.50	15.53 ± 1.69	4.716	0.2287	1	435 ± 109	7
XCC J0223.9-0830	35.9826	−8.5069	0.16	2.78 ± 1.20	3.96 ± 0.96	4.43 ± 1.08	4.69 ± 0.70	4.218	0.1635	1	407 ± 214	9
XCC J0224.0-0835	35.998	−8.5956	0.27	15.75 ± 3.01	39.57 ± 1.97	130.36 ± 6.49	37.44 ± 1.18	5.514	0.2701	1	675 ± 142	10
XCC J0224.1-0816	36.0234	−8.2682	0.26	5.76 ± 2.36	6.63 ± 2.74	21.38 ± 8.85	11.87 ± 2.94	3.876	···	2	···	...
XCC J0224.3-0917	36.0903	−9.289	0.67	0.44 ± 0.70	2.05 ± 0.66	59.62 ± 19.29	15.85 ± 3.11	2.094	···	2	···	...
XCC J0224.4-0924	36.0983	−9.4054	0.49	2.85 ± 1.22	1.92 ± 0.57	27.29 ± 8.18	11.37 ± 2.08	2.346	0.4874	2	···	1
XCC J0224.4-0827	36.1046	−8.4578	0.09	1.93 ± 3.97	9.66 ± 6.04	2.91 ± 1.82	3.79 ± 1.38	6.738	···	2	···	...
XCC J0224.6-0931	36.1586	−9.5279	0.71	1.38 ± 1.17	2.23 ± 0.66	73.34 ± 21.69	17.43 ± 3.14	2.076	···	2	···	...
XCC J0224.6-0919	36.1606	−9.3302	1.08	2.01 ± 0.94	2.02 ± 1.13	170.78 ± 96.03	21.25 ± 7.02	1.698	···	2	···	...
XCC J0224.7-0924	36.1888	−9.4073	0.93	0.88 ± 0.43	1.63 ± 0.65	101.87 ± 40.78	17.52 ± 4.21	1.746	···	2	···	...
XCC J0224.8-0620	36.2207	−6.3371	1.05	7.75 ± 0.47	1.35 ± 0.37	113.31 ± 31.63	16.80 ± 2.86	1.596	···	2	···	...
XCC J0225.0-0950	36.2713	−9.8381	0.15	9.79 ± 2.70	34.41 ± 1.79	36.81 ± 1.91	18.22 ± 0.60	6.786	0.1594	1	528 ± 69	18
XCC J0225.2-0623	36.3021	−6.3837	0.2	7.78 ± 1.73	18.65 ± 1.55	34.42 ± 2.86	16.85 ± 0.88	5.334	0.2041	1	414 ± 78	10
XCC J0225.5-0619	36.3929	−6.3228	0.95	2.76 ± 0.66	1.44 ± 0.66	95.43 ± 44.13	16.50 ± 4.54	1.686	···	2	···	...
XCC J0225.5-0612	36.3953	−6.2134	0.31	2.77 ± 1.66	3.87 ± 1.67	16.58 ± 7.17	9.81 ± 2.53	3.3	0.2932	2	···	1
XCC J0225.6-0946	36.4034	−9.7797	0.34	5.84 ± 1.95	2.24 ± 0.81	13.93 ± 5.05	8.41 ± 1.84	2.766	0.3429	1	452 ± 152	5
XCC J0225.9-0830	36.479	−8.5086	1.05	0.75 ± 0.28	1.51 ± 0.61	124.59 ± 50.99	17.85 ± 4.38	1.632	···	2	···	...
XCC J0226.4-0845	36.6144	−8.766	0.33	2.84 ± 1.18	2.70 ± 1.88	15.29 ± 10.64	9.02 ± 3.63	2.922	···	2	···	...
XCC J0229.0-0549	37.2606	−5.8297	1.02	0.21 ± 0.53	0.76 ± 0.42	64.61 ± 36.26	12.05 ± 3.97	1.458	···	2	···	...
XCC J0229.2-0553	37.3203	−5.8983	0.3	1.75 ± 1.16	5.21 ± 0.57	21.88 ± 2.42	11.73 ± 0.81	3.522	0.2915	1	505 ± 94	7
XCC J0229.5-0553	37.3826	−5.8998	0.3	4.75 ± 1.93	3.31 ± 0.41	14.46 ± 1.79	8.97 ± 0.69	3.186	0.295	1	322 ± 64	13
XCC J0230.1-0540	37.5371	−5.6803	0.47	7.84 ± 4.63	2.84 ± 0.87	41.40 ± 12.69	14.7 ± 2.74	2.514	0.4991	1	···	3
XCC J0230.8-0421	37.7203	−4.3507	0.16	2.78 ± 2.09	11.74 ± 1.96	9.63 ± 1.61	7.83 ± 0.81	5.712	0.1408	1	427 ± 132	9
XCC J0230.9-0431	37.7413	−4.5285	0.39	0.87 ± 0.93	3.41 ± 2.14	28.08 ± 17.65	12.64 ± 4.63	2.868	···	2	···	...
XCC J0231.7-0452	37.927	−4.8814	0.2	24.78 ± 1.22	128.74 ± 3.52	183.53 ± 5.02	49.94 ± 0.87	8.328	0.1852	1	426 ± 194	9
XCC J0232.6-0449	38.1654	−4.8331	0.17	2.76 ± 1.67	5.70 ± 2.33	7.04 ± 2.88	6.27 ± 1.53	4.494	···	2	···	...

Table 5
(Continued)

ID *XMM*-CFHTLS	R.A. (deg)	Decl. (deg)	R.S. z	α	X-ray Flux 10^{-14} erg cm^{-2} s^{-1}	L_X 10^{42} erg s^{-1}	M_{200c} 10^{13} $M_\odot$	r_{200c} arcmin	specz	Visual Flag	$\sigma(v)$ (km s^{-1})	N_σ
(1)	(2)	(3)	(4)	(5)	(6)	(7)	(8)	(9)	(10)	(11)	(12)	(13)
XCC J0233.4-0540	38.3625	−5.6749	0.51	3.82 ± 1.30	2.52 ± 0.63	42.21 ± 10.66	14.48 ± 2.24	2.4	0.5287	1	···	4
XCC J0233.6-0542	38.4048	−5.701	0.3	2.75 ± 1.65	2.42 ± 0.87	11.02 ± 3.99	7.51 ± 1.64	2.964	···	2	···	···
XCC J0233.6-0941	38.4183	−9.6995	0.26	5.76 ± 1.18	11.33 ± 1.48	37.40 ± 4.89	16.91 ± 1.38	4.302	0.2646	1	395 ± 56	20
XCC J0233.8-0939	38.4607	−9.6656	0.25	1.80 ± 1.34	4.41 ± 1.50	15.54 ± 5.30	9.60 ± 1.98	3.51	0.2695	1	475 ± 117	7
XCC J0234.3-0940	38.5794	−9.6711	0.79	20.41 ± 3.94	12.28 ± 1.78	439.67 ± 63.87	50.91 ± 4.61	2.766	···	1	···	···
XCC J0234.3-0936	38.5851	−9.6158	1.09	2.70 ± 1.00	3.00 ± 0.98	247.16 ± 81.09	26.68 ± 5.31	1.824	···	2	···	···
XCC J0234.3-0951	38.586	−9.8583	0.65	13.51 ± 1.13	14.29 ± 2.40	291.32 ± 48.93	46.18 ± 4.82	3.18	0.6119	1	···	4
XCC J0234.7-0548	38.6768	−5.8095	1.0	0.4 ± 0.58	2.59 ± 1.18	179.6 ± 82.2	23.62 ± 6.44	1.842	···	2	···	···
XCC J0234.9-0400	38.7257	−4.013	0.61	1.58 ± 1.42	0.90 ± 0.35	22.80 ± 8.84	9.06 ± 2.11	1.854	···	2	···	···
XCC J0849.2-0252	132.307	−2.8775	0.25	7.80 ± 2.10	11.30 ± 1.56	26.36 ± 3.65	13.96 ± 1.20	4.602	0.2259	1	491 ± 124	11
XCC J0849.9-0312	132.473	−3.2009	0.6	4.57 ± 1.35	2.18 ± 0.84	49.22 ± 18.94	14.96 ± 3.46	2.214	···	1	···	···
XCC J0849.9-0159	132.491	−1.9925	0.05	0.97 ± 0.98	28.05 ± 10.69	2.44 ± 0.93	3.48 ± 0.80	11.394	···	2	···	···
XCC J0850.0-0149	132.5	−1.8261	0.38	3.86 ± 1.27	1.09 ± 0.32	8.80 ± 2.61	6.07 ± 1.09	2.292	···	1	···	···
XCC J0850.0-0235	132.504	−2.5955	0.22	5.8 ± 2.07	6.01 ± 2.96	14.19 ± 6.98	9.39 ± 2.74	4.032	0.226	1	···	3
XCC J0850.1-0149	132.53	−1.8279	1.02	8.21 ± 0.99	0.68 ± 0.18	58.78 ± 16.23	11.34 ± 1.91	1.428	···	2	···	···
XCC J0850.7-0140	132.674	−1.682	0.26	2.76 ± 1.02	2.66 ± 1.06	8.65 ± 3.46	6.65 ± 1.60	3.198	···	1	···	···
XCC J0852.0-0134	133.022	−1.5738	0.61	4.58 ± 1.21	2.93 ± 1.27	67.02 ± 29.12	18.06 ± 4.69	2.334	···	1	···	···
XCC J0852.2-0533	133.066	−5.5651	0.21	21.79 ± 3.64	88.92 ± 2.82	133.65 ± 4.24	40.64 ± 0.82	7.638	0.1891	1	385 ± 85	7
XCC J0852.2-0101	133.067	−1.0261	0.49	12.85 ± 1.99	28.46 ± 1.36	298.44 ± 14.35	53.97 ± 1.64	4.122	0.4587	1	···	4
XCC J0852.4-0345	133.118	−3.752	0.98	5.56 ± 0.38	3.09 ± 1.09	200.94 ± 71.07	25.85 ± 5.52	1.926	···	2	···	···
XCC J0852.5-0112	133.123	−1.2128	0.57	9.79 ± 2.68	4.75 ± 1.37	89.64 ± 25.91	22.58 ± 3.98	2.634	···	1	···	···
XCC J0852.6-0152	133.154	−1.8826	0.81	3.31 ± 1.62	2.49 ± 1.25	108.55 ± 54.40	20.41 ± 6.06	2.01	···	2	···	···
XCC J0852.9-0503	133.236	−5.0593	0.06	3.97 ± 4.75	21.01 ± 5.00	1.33 ± 0.31	2.37 ± 0.34	11.592	0.043	1	300 ± 100	9
XCC J0853.0-0344	133.269	−3.7363	0.94	26.82 ± 2.07	3.76 ± 0.82	218.92 ± 47.64	28.33 ± 3.80	2.034	···	1	···	···
XCC J0853.1-0459	133.282	−4.9996	0.45	1.86 ± 1.36	1.65 ± 0.70	19.57 ± 8.39	9.51 ± 2.44	2.346	···	2	···	···
XCC J0853.3-0144	133.333	−1.7485	0.62	10.55 ± 1.39	1.59 ± 0.54	39.87 ± 13.64	12.84 ± 2.66	2.058	···	1	···	···
XCC J0853.4-0341	133.361	−3.6866	0.73	6.35 ± 0.97	5.01 ± 0.94	162.38 ± 30.58	28.46 ± 3.32	2.4	···	1	···	···
XCC J0853.6-0348	133.403	−3.8094	0.85	7.16 ± 0.57	1.23 ± 0.42	64.58 ± 22.21	14.10 ± 2.93	1.722	···	1	···	···
XCC J0853.6-0532	133.416	−5.543	0.61	1.58 ± 0.74	0.91 ± 0.26	23.07 ± 6.65	9.13 ± 1.60	1.86	···	2	···	···
XCC J0853.9-0503	133.484	−5.0618	0.36	2.87 ± 2.51	1.80 ± 0.66	12.60 ± 4.64	7.77 ± 1.72	2.598	···	2	···	···
XCC J0854.1-0342	133.524	−3.7154	0.73	8.35 ± 1.68	4.26 ± 1.28	139.87 ± 42.23	25.87 ± 4.75	2.328	···	1	···	···
XCC J0854.2-0221	133.555	−2.3499	0.37	12.87 ± 3.88	22.48 ± 1.77	147.73 ± 11.66	37.30 ± 1.85	4.308	0.3679	1	451 ± 133	9
XCC J0854.8-0530	133.702	−5.4999	0.06	0.97 ± 2.91	4.95 ± 1.53	0.64 ± 0.19	1.47 ± 0.27	7.188	···	2	···	···
XCC J0854.9-0147	133.743	−1.7927	0.74	2.34 ± 0.69	1.09 ± 0.35	42.34 ± 13.71	11.93 ± 2.34	1.782	···	2	···	···
XCC J0856.4-0146	134.105	−1.7725	0.15	2.79 ± 1.75	5.34 ± 1.86	4.95 ± 1.72	5.08 ± 1.07	4.674	···	2	···	···
XCC J0857.1-0106	134.293	−1.1138	0.63	6.54 ± 1.79	1.94 ± 0.55	45.78 ± 13.14	14.16 ± 2.48	2.154	0.609	1	···	1
XCC J0857.4-0532	134.367	−5.5371	0.08	0.95 ± 0.97	11.57 ± 4.55	2.71 ± 1.06	3.64 ± 0.86	7.416	···	2	···	···
XCC J0858.3-0438	134.595	−4.6448	0.71	14.38 ± 0.69	3.33 ± 0.73	105.18 ± 23.25	21.96 ± 2.99	2.244	···	1	···	···
XCC J0858.6-0525	134.661	−5.4212	0.09	8.93 ± 2.81	37.10 ± 2.22	11.63 ± 0.69	9.19 ± 0.34	9.048	···	1	···	···
XCC J0859.7-0419	134.923	−4.3263	0.75	2.55 ± 1.50	1.22 ± 0.67	48.06 ± 26.64	12.81 ± 4.17	1.806	···	2	···	···
XCC J0900.3-0318	135.083	−3.3071	0.15	4.79 ± 1.07	2.29 ± 0.79	2.09 ± 0.72	2.92 ± 0.61	3.888	···	2	···	···
XCC J0901.5-0139	135.377	−1.6532	0.34	10.84 ± 3.01	50.38 ± 3.53	231.1 ± 16.20	51.94 ± 2.30	5.412	0.3163	1	456 ± 69	20
XCC J0901.6-0154	135.406	−1.9074	0.29	6.73 ± 1.95	5.18 ± 0.32	25.91 ± 1.63	12.81 ± 0.51	3.408	0.3151	1	454 ± 46	7
XCC J0901.6-0158	135.415	−1.9799	0.36	8.87 ± 3.70	6.28 ± 0.31	30.95 ± 1.56	14.37 ± 0.46	3.546	0.3141	1	516 ± 80	11
XCC J0901.7-0228	135.437	−2.4809	0.93	1.88 ± 1.11	3.32 ± 1.15	190.98 ± 66.45	26.20 ± 5.51	1.998	···	2	···	···
XCC J0901.7-0208	135.439	−2.1378	0.42	5.84 ± 3.06	1.47 ± 0.28	13.29 ± 2.58	7.77 ± 0.93	2.394	0.3994	1	334 ± 64	5
XCC J0901.8-0143	135.45	−1.7226	0.25	5.80 ± 1.09	8.33 ± 2.34	24.49 ± 6.87	13.06 ± 2.23	4.134	···	2	···	···
XCC J0901.9-0200	135.494	−2.0115	1.01	18.30 ± 1.74	1.06 ± 0.15	84.33 ± 12.14	14.42 ± 1.29	1.554	···	2	···	···
XCC J0902.0-0228	135.5	−2.4734	0.95	0.76 ± 1.03	2.75 ± 1.45	169.29 ± 89.67	23.81 ± 7.44	1.908	···	2	···	···
XCC J0902.3-0230	135.582	−2.5034	0.36	0.87 ± 0.93	5.90 ± 2.84	39.50 ± 19.00	16.15 ± 4.61	3.312	···	2	···	···
XCC J0902.4-0219	135.604	−2.3188	0.3	1.75 ± 1.16	2.58 ± 0.90	11.74 ± 4.11	7.82 ± 1.66	3.006	···	2	···	···
XCC J0903.5-0518	135.873	−5.3151	0.19	2.79 ± 2.04	3.17 ± 1.21	4.99 ± 1.91	4.95 ± 1.14	3.774	···	2	···	···
XCC J0904.0-0151	136.01	−1.8636	0.72	2.34 ± 0.67	6.45 ± 2.54	198.57 ± 78.17	32.68 ± 7.73	2.538	···	2	···	···
XCC J0904.0-0142	136.02	−1.7036	0.26	1.76 ± 1.32	11.66 ± 4.01	36.98 ± 12.73	16.86 ± 3.51	4.356	···	2	···	···
XCC J0904.1-0329	136.026	−3.492	0.71	1.38 ± 0.60	1.76 ± 0.67	59.28 ± 22.66	15.21 ± 3.50	1.986	···	2	···	···
XCC J0904.1-0202	136.043	−2.0333	0.29	7.73 ± 0.97	14.88 ± 4.81	58.20 ± 18.83	22.02 ± 4.32	4.392	0.2874	1	546 ± 70	17
XCC J0904.6-0202	136.154	−2.0496	0.41	7.85 ± 3.07	9.31 ± 3.42	80.48 ± 29.58	24.4 ± 5.41	3.45	0.4087	1	553 ± 243	5
XCC J0904.6-0200	136.161	−2.0138	1.03	7.10 ± 0.90	5.18 ± 1.65	356.26 ± 113.66	35.62 ± 6.90	2.076	···	2	···	···
XCC J2202.1+0142	330.539	1.716	0.21	4.79 ± 1.23	6.05 ± 2.03	13.41 ± 4.51	9.10 ± 1.85	4.08	0.2199	2	522 ± 153	10
XCC J2206.3+0146	331.576	1.7725	1.04	5.96 ± 0.81	1.76 ± 0.78	139.47 ± 61.86	19.36 ± 5.12	1.686	···	2	···	···
XCC J2206.4+0139	331.603	1.6554	0.32	8.80 ± 1.09	7.33 ± 1.49	28.21 ± 5.75	13.92 ± 1.75	3.828	0.2818	1	···	1
XCC J2212.1-0010	333.029	−0.168	0.8	4.35 ± 1.19	2.11 ± 1.10	90.77 ± 47.42	18.37 ± 5.67	1.956	···	2	···	···

Table 5
(Continued)

ID *XMM*-CFHTLS	R.A. (deg)	Decl. (deg)	R.S. z	α	X-ray Flux 10^{-14} erg cm^{-2} s^{-1}	L_X 10^{42} erg s^{-1}	M_{200c} 10^{13} $M_\odot$	r_{200c} arcmin	specz	Visual Flag	$\sigma(v)$ (km s^{-1})	N_σ
(1)	(2)	(3)	(4)	(5)	(6)	(7)	(8)	(9)	(10)	(11)	(12)	(13)
XCC J2212.1-0008	333.045	−0.1348	0.36	4.87 ± 3.30	5.61 ± 1.01	38.75 ± 7.02	15.88 ± 1.78	3.264	0.3647	1	···	3
XCC J2212.2+0005	333.072	0.0957	0.8	1.35 ± 1.02	2.01 ± 1.06	86.90 ± 46.13	17.87 ± 5.59	1.938	···	1	···	···
XCC J2214.3+0047	333.59	0.7857	0.32	8.80 ± 1.09	3.56 ± 0.76	18.72 ± 4.00	10.36 ± 1.36	3.132	0.3202	1	···	2
XCC J2214.8+0047	333.706	0.7837	0.34	5.84 ± 2.29	3.92 ± 0.57	19.83 ± 2.90	10.79 ± 0.98	3.21	0.3155	1	···	3
XCC J2214.9-0039	333.736	−0.6541	0.9	6.96 ± 0.73	2.53 ± 1.12	139.33 ± 61.74	22.02 ± 5.82	1.926	···	2	···	···
XCC J2217.7+0017	334.436	0.2914	0.71	2.38 ± 1.70	0.48 ± 0.07	18.29 ± 2.72	7.17 ± 0.66	1.548	···	2	···	···
XCC J2217.8+0023	334.458	0.3835	0.91	5.93 ± 1.87	0.27 ± 0.06	20.62 ± 4.69	6.42 ± 0.90	1.266	···	1	···	···
XCC J2217.8+0016	334.471	0.279	0.83	1.23 ± 0.51	0.17 ± 0.04	10.76 ± 2.57	4.56 ± 0.67	1.2	···	2	···	···
XCC J0210.4-0345	32.6203	−3.7545	0.54	3.77 ± 1.04	0.94 ± 0.34	17.85 ± 6.56	8.26 ± 1.83	1.956	···	2	···	···
XCC J0211.0-0853	32.7522	−8.8984	0.45	8.86 ± 2.41	1.81 ± 0.87	21.06 ± 10.11	10.00 ± 2.85	2.4	0.4459	2	···	1
XCC J0214.1-0808	33.5342	−8.1451	0.25	2.80 ± 1.67	2.90 ± 1.01	8.57 ± 2.98	6.67 ± 1.40	3.312	0.2495	1	180 ± 55	13
XCC J0214.7-0618	33.676	−6.309	0.25	5.80 ± 1.79	3.06 ± 1.31	8.23 ± 3.53	6.55 ± 1.68	3.408	0.2395	1	528 ± 30	25
XCC J0214.7-0804	33.6919	−8.069	0.7	3.39 ± 1.54	0.86 ± 0.62	29.99 ± 21.66	9.93 ± 4.13	1.74	···	1	···	···
XCC J0215.0-0626	33.764	−6.4469	0.2	0.78 ± 1.73	9.97 ± 3.85	2.43 ± 0.94	3.40 ± 0.79	7.11	0.0817	1	···	···
XCC J0216.1-0702	34.0324	−7.0483	0.43	6.85 ± 1.22	0.80 ± 0.40	7.86 ± 3.91	5.49 ± 1.62	2.088	0.4114	1	232 ± 74	9
XCC J0216.7-0648	34.1805	−6.8093	0.19	2.79 ± 2.04	3.19 ± 1.48	5.01 ± 2.32	4.97 ± 1.37	3.774	···	2	···	···
XCC J0216.7-0935	34.1859	−9.585	0.58	5.78 ± 1.73	0.69 ± 0.34	16.70 ± 8.22	7.53 ± 2.20	1.776	0.5941	1	···	3
XCC J0216.8-0918	34.2012	−9.3103	0.73	11.35 ± 0.68	2.95 ± 1.46	78.05 ± 38.83	19.15 ± 5.64	2.274	0.652	2	···	3
XCC J0219.3-0735	34.8297	−7.5998	0.58	9.78 ± 2.73	2.37 ± 0.69	47.02 ± 13.73	14.96 ± 2.66	2.304	0.5684	1	···	2
XCC J0221.5-0626	35.394	−6.4377	0.3	7.75 ± 1.65	2.10 ± 0.86	10.67 ± 4.37	7.27 ± 1.78	2.826	0.314	1	···	2
XCC J0222.2-0617	35.5689	−6.2946	0.75	2.55 ± 1.59	1.27 ± 0.67	53.36 ± 28.24	13.43 ± 4.19	1.8	0.7716	2	···	1
XCC J0223.5-0828	35.8887	−8.4739	0.25	5.80 ± 1.09	0.50 ± 0.63	1.98 ± 2.47	2.54 ± 1.72	2.166	0.2826	1	333 ± 72	13
XCC J0224.4-0915	36.1137	−9.2658	0.33	1.84 ± 2.27	2.93 ± 1.29	16.56 ± 7.29	9.50 ± 2.49	2.97	···	2	···	···
XCC J0225.7-0828	36.4279	−8.4744	0.52	3.80 ± 1.09	1.62 ± 1.19	31.10 ± 22.95	11.65 ± 4.94	2.16	0.5531	2	···	2
XCC J0230.9-0418	37.7467	−4.3051	0.14	1.80 ± 1.09	5.02 ± 2.49	4.16 ± 2.06	4.57 ± 1.34	4.716	0.1428	1	396 ± 119	5
XCC J0233.3-0550	38.3245	−5.8364	0.32	1.80 ± 1.34	1.65 ± 1.49	8.02 ± 7.24	6.08 ± 3.10	2.7	0.3086	2	···	3
XCC J0233.8-0543	38.4688	−5.7187	0.39	3.87 ± 2.14	1.07 ± 0.48	7.37 ± 3.30	5.53 ± 1.47	2.334	0.3566	2	···	4
XCC J0234.7-0542	38.6846	−5.7055	0.12	0.80 ± 1.09	4.09 ± 2.70	3.28 ± 2.16	3.93 ± 1.50	4.53	0.1412	1	···	1
XCC J0849.2-0157	132.309	−1.9545	0.2	0.78 ± 0.88	1.64 ± 0.63	2.87 ± 1.10	3.44 ± 0.79	3.198	···	2	···	···
XCC J0850.3-0324	132.593	−3.4152	0.52	5.80 ± 1.26	2.71 ± 1.53	46.82 ± 26.56	15.36 ± 5.11	2.418	0.537	1	···	3
XCC J0850.4-0312	132.61	−3.2091	0.45	5.86 ± 2.41	2.21 ± 0.89	29.85 ± 12.10	12.14 ± 2.95	2.43	0.4789	1	···	2
XCC J0851.2-0528	132.806	−5.4789	0.83	6.23 ± 0.51	2.34 ± 1.15	108.65 ± 53.76	20.02 ± 5.87	1.962	0.8311	1	···	1
XCC J0851.4-0532	132.861	−5.5427	0.22	1.8 ± 1.08	2.43 ± 1.09	9.14 ± 4.13	6.79 ± 1.83	3.06	0.2768	2	···	3
XCC J0851.4-0537	132.869	−5.6233	0.72	2.34 ± 2.00	2.02 ± 1.01	69.06 ± 34.56	16.62 ± 4.92	2.028	···	2	···	···
XCC J0851.5-0104	132.884	−1.0747	0.8	3.35 ± 2.13	1.11 ± 1.24	51.49 ± 57.04	12.78 ± 7.81	1.734	···	2	···	···
XCC J0851.5-0451	132.893	−4.8642	0.06	0.97 ± 3.36	9.00 ± 3.79	2.05 ± 0.86	3.05 ± 0.77	7.062	0.0792	1	···	2
XCC J0851.6-0451	132.913	−4.8567	0.62	6.55 ± 1.39	1.79 ± 1.01	46.06 ± 26.01	13.93 ± 4.62	2.088	0.6309	1	···	2
XCC J0851.9-0507	132.981	−5.1185	0.39	4.87 ± 1.31	5.39 ± 3.18	45.42 ± 26.81	17.08 ± 5.90	3.126	0.3981	1	···	4
XCC J0852.8-0152	133.203	−1.8718	0.93	2.88 ± 1.22	1.34 ± 0.95	85.73 ± 61.03	15.69 ± 6.44	1.686	···	1	···	···
XCC J0852.8-0137	133.219	−1.6214	0.39	8.87 ± 1.51	2.44 ± 0.76	20.45 ± 6.39	10.32 ± 1.96	2.682	···	1	···	···
XCC J0852.9-0529	133.244	−5.493	0.58	8.78 ± 2.12	4.53 ± 2.09	89.27 ± 41.30	22.31 ± 6.14	2.592	···	1	···	···
XCC J0853.1-0348	133.296	−3.8084	0.8	4.35 ± 1.19	1.56 ± 0.49	69.43 ± 21.88	15.47 ± 2.96	1.848	···	2	···	···
XCC J0853.8-0223	133.448	−2.392	0.36	2.87 ± 1.31	2.87 ± 1.83	24.40 ± 15.57	11.52 ± 4.27	2.76	0.3938	2	···	3
XCC J0854.5-0140	133.646	−1.6745	0.62	6.55 ± 2.49	3.36 ± 1.37	68.67 ± 28.14	18.81 ± 4.62	2.442	0.5833	1	···	1
XCC J0855.7-0146	133.933	−1.7745	0.52	0.80 ± 2.53	1.09 ± 0.33	20.03 ± 6.20	8.92 ± 1.68	2.022	···	2	···	···
XCC J0856.4-0136	134.098	−1.6031	0.45	4.86 ± 2.06	2.33 ± 0.60	26.40 ± 6.83	11.58 ± 1.83	2.526	0.4443	1	···	3
XCC J0856.4-0107	134.122	−1.1329	0.58	4.78 ± 1.06	1.22 ± 0.78	26.80 ± 17.27	10.33 ± 3.87	2.004	···	1	···	···
XCC J0858.1-0342	134.532	−3.7164	0.77	2.50 ± 0.79	1.60 ± 0.59	65.22 ± 24.15	15.29 ± 3.41	1.884	···	2	···	···
XCC J0858.9-0433	134.737	−4.5637	0.09	1.93 ± 1.72	4.40 ± 3.04	1.32 ± 0.91	2.28 ± 0.91	5.688	···	1	···	···
XCC J0859.4-0432	134.872	−4.5438	0.11	0.84 ± 0.91	8.17 ± 2.95	3.82 ± 1.38	4.44 ± 0.96	5.904	···	1	···	···
XCC J0859.6-0416	134.906	−4.2764	0.14	0.80 ± 1.09	2.54 ± 1.06	1.98 ± 0.83	2.85 ± 0.71	4.104	···	2	···	···
XCC J0859.9-0422	134.993	−4.3686	0.16	5.78 ± 2.09	11.66 ± 5.25	12.70 ± 5.72	9.22 ± 2.47	5.388	···	1	···	···
XCC J0900.7-0306	135.173	−3.1143	0.25	4.80 ± 2.19	3.32 ± 0.85	8.08 ± 2.08	6.53 ± 1.03	3.528	0.2292	1	···	4
XCC J0901.7-0138	135.435	−1.6384	0.3	9.75 ± 1.16	6.77 ± 2.06	30.01 ± 9.14	14.26 ± 2.64	3.672	···	1	···	···
XCC J0902.3-0226	135.583	−2.4422	0.14	1.80 ± 1.34	6.22 ± 2.16	4.96 ± 1.72	5.12 ± 1.07	4.986	···	1	···	···
XCC J0902.8-0213	135.708	−2.2305	0.94	3.82 ± 0.69	1.58 ± 1.33	101.26 ± 85.60	17.30 ± 8.30	1.728	···	1	···	···
XCC J0903.1-0537	135.793	−5.6259	0.3	2.75 ± 1.16	5.41 ± 3.69	24.16 ± 16.5	12.41 ± 4.90	3.504	···	1	···	···
XCC J0904.0-0343	136.0	−3.7195	1.0	11.4 ± 1.22	1.44 ± 0.51	107.14 ± 38.14	16.97 ± 3.65	1.65	···	1	···	···
XCC J0904.2-0158	136.065	−1.9808	0.15	2.79 ± 1.07	15.31 ± 8.29	14.47 ± 7.83	10.10 ± 3.22	5.88	···	1	···	···
XCC J2200.4+0058	330.103	0.9804	0.09	1.93 ± 1.72	6.93 ± 3.67	2.64 ± 1.39	3.53 ± 1.10	5.94	0.1005	2	···	3
XCC J2200.9+0125	330.241	1.4297	0.09	0.93 ± 1.72	8.21 ± 2.99	3.87 ± 1.41	4.48 ± 0.98	5.898	0.1105	1	356 ± 177	6
XCC J2201.4+0152	330.37	1.8668	0.19	2.79 ± 1.23	4.88 ± 2.59	4.46 ± 2.36	4.75 ± 1.49	4.596	0.1492	2	···	1
XCC J2202.3+0148	330.573	1.8152	0.19	0.79 ± 1.23	2.25 ± 1.45	3.51 ± 2.27	3.95 ± 1.48	3.498	···	1	···	···

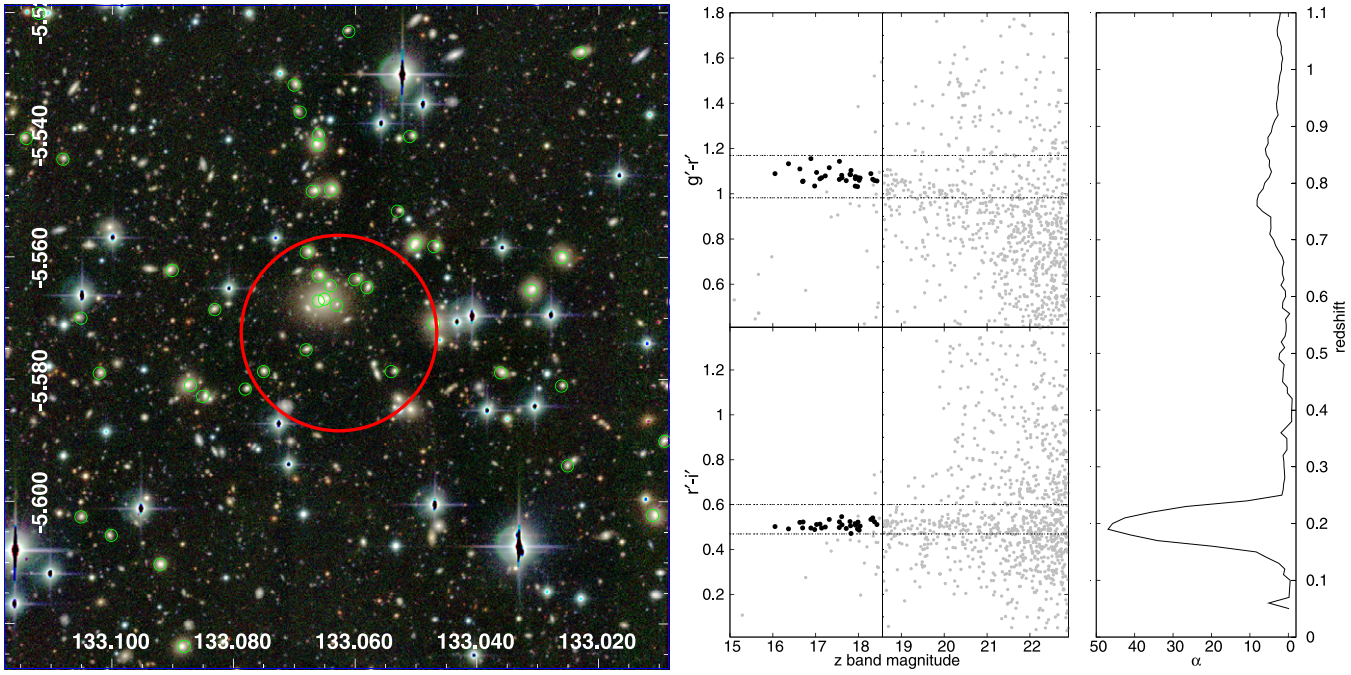

Figure 15. Same as in Figure 6, but for an RASS cluster at a redshift of 0.19. The position of the RASS source is shown by a large red circle with a radius of 1′.

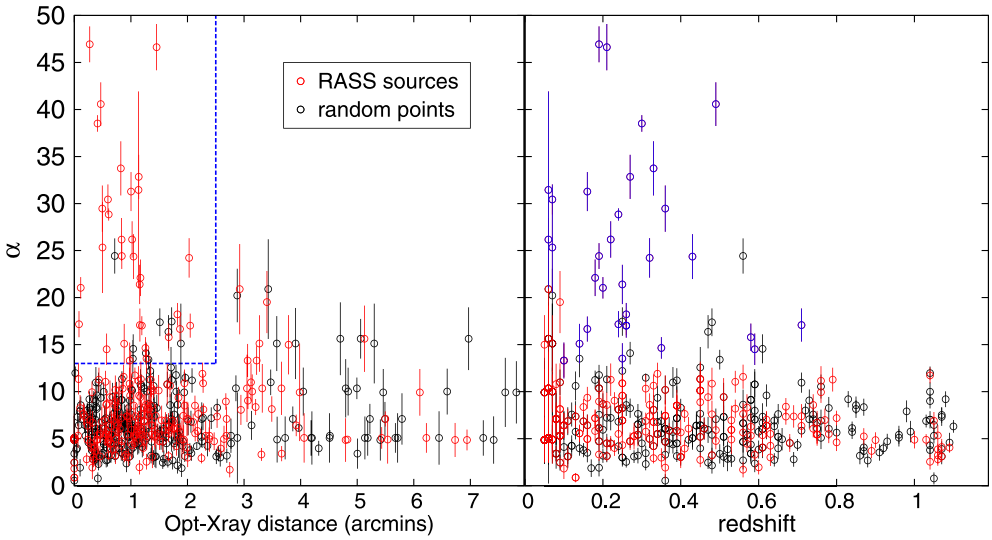

Figure 16. Left: red sequence significance, α, vs. redshift for RASS X-ray sources. Right: red sequence significance, α, vs. offset between optical and X-ray cluster centers. Red circles mark the RASS X-ray sources, and black circles are random sources in CFHTLS. A blue dashed line shows the criteria for selection of clusters among the RASS sources. Right: α vs. the redshift for the RASS and random sources. In this panel, blue circles are the RASS clusters.

Table 5
(Continued)

ID *XMM*-CFHTLS (1)	R.A. (deg) (2)	Decl. (deg) (3)	R.S. z (4)	α (5)	X-ray Flux 10^{-14} erg cm^{-2} s^{-1} (6)	L_X 10^{42} erg s^{-1} (7)	M_{200c} 10^{13} $M_\odot$ (8)	r_{200c} arcmin (9)	specz (10)	Visual Flag (11)	$\sigma(v)$ (km s^{-1}) (12)	N_σ (13)
XCC J2204.5+0239	331.131	2.6648	0.58	5.78 ± 1.06	2.63 ± 0.89	67.63 ± 22.99	17.66 ± 3.63	2.238	0.6404	1	...	1
XCC J2210.4+0203	332.605	2.0554	0.74	12.34 ± 1.14	1.58 ± 0.70	59.09 ± 26.29	14.76 ± 3.92	1.914	...	2	...	...
XCC J2211.3+0200	332.832	2.0111	0.46	5.85 ± 1.99	3.06 ± 2.02	37.17 ± 24.62	14.19 ± 5.45	2.628	0.4617	2	...	2
XCC J2211.3+0000	332.834	0.0103	0.81	3.31 ± 0.66	0.61 ± 0.28	30.88 ± 14.34	9.13 ± 2.52	1.536	...	2	...	...
XCC J2211.9-0001	332.981	−0.0311	0.06	2.97 ± 3.36	7.09 ± 6.51	0.90 ± 0.83	1.83 ± 0.94	7.734	...	2	...	...
XCC J2214.0+0057	333.512	0.9574	0.76	8.53 ± 0.83	1.65 ± 1.04	65.15 ± 41.12	15.42 ± 5.67	1.908	...	1	...	...
XCC J2214.0-0055	333.52	−0.9273	0.25	4.80 ± 2.10	2.16 ± 0.90	4.77 ± 1.99	4.69 ± 1.17	3.264	0.2207	1	...	4
XCC J2217.0+0016	334.258	0.2693	0.96	7.71 ± 0.76	0.08 ± 0.03	9.12 ± 3.90	3.64 ± 0.93	1.014	...	2	...	...

(This table is available in its entirety in machine-readable form.)

Table 6
Catalog of RASS-CFHTLS X-ray-selected Galaxy Clusters

ID RASS-CFHTLS (1)	R.A. (deg) (2)	Decl. (deg) (3)	R.S. z (4)	α (5)	Opt. R.A. (deg) (6)	Opt. Decl. (deg) (7)	X-ray Flux 10^{-13} erg cm^{-2} s^{-1} (8)	L_X 10^{42} erg s^{-1} (9)	specz (10)	$\sigma(v)$ (km s^{-1}) (11)	N_σ (12)	log[$L_X(L_S)$] erg s^{-1} (13)
RCC J0202.7-0700	30.556	−7.00291	0.06	26.1 ± 2.2	30.5658	−7.01287	12.05 ± 2.98	15.0 ± 3.78	···	···	···	43.0297
RCC J0203.2-0949	30.8715	−9.82674	0.33	33.7 ± 2.9	30.859	−9.82075	5.15 ± 1.38	325.6 ± 80.3	0.3216	···	1	43.9727
RCC J0204.6-0931	31.151	−9.53	0.58	15.8 ± 1.5	31.179	−9.52669	1.11 ± 0.59	253.4 ± 141.3	0.6232	···	2	43.7222
RCC J0205.2-0544	31.3627	−5.7708	0.32	24.2 ± 2.1	31.3708	−5.73796	3.15 ± 1.12	156.9 ± 53.2	0.2972	···	2	44.0285
RCC J0206.6-0943	31.5231	−9.74276	0.1	13.3 ± 1.9	31.5168	−9.72768	2.36 ± 1.09	7.8 ± 3.4	0.0857	···	4	43.0459
RCC J0208.6-0554	32.0915	−5.90348	0.07	25.3 ± 4.8	32.0871	−5.91055	2.91 ± 1.35	4.2 ± 2.2	···	···	···	43.3055
RCC J0210.9-0633	32.6952	−6.58427	0.06	31.4 ± 10.5	32.6897	−6.56617	7.82 ± 1.82	4.6 ± 1.7	0.0416	···	1	43.4136
RCC J0211.0-0454	32.7836	−4.9044	0.14	15.1 ± 2.1	32.7694	−4.90051	1.52 ± 0.78	11.8 ± 6.4	0.1379	···	3	43.3059
RCC J0214.9-0627	33.6162	−6.47615	0.24	28.8 ± 0.6	33.6165	−6.46603	4.00 ± 1.40	65.0 ± 27.7	0.2366	344 ± 93	13	43.857
RCC J0214.0-0433	33.661	−4.56333	0.16	31.3 ± 2.1	33.6726	−4.55127	8.18 ± 1.76	93.9 ± 20.7	0.1456	···	4	44.023
RCC J0214.6-0355	33.6875	−3.94368	0.16	16.7 ± 1.3	33.7144	−3.92789	16.60 ± 3.19	96.0 ± 20.5	0.1402	···	1	43.601
RCC J0214.3-0349	33.7193	−3.83385	0.71	17.1 ± 1.8	33.7035	−3.82267	2.68 ± 1.19	583.4 ± 270.8	···	···	···	44.0768
RCC J0221.5-0545	35.5108	−5.76391	0.26	17.0 ± 1.0	35.4915	−5.75868	2.03 ± 0.94	92.0 ± 37.1	0.2591	···	2	43.4434
RCC J0223.3-0851	35.8678	−8.86884	0.19	24.4 ± 1.4	35.8689	−8.85491	2.13 ± 0.93	46.2 ± 16.5	0.1632	381 ± 154	5	43.6504
RCC J0223.8-0857	35.8981	−8.98174	0.43	24.4 ± 2.4	35.8944	−8.96471	1.76 ± 0.87	92.7 ± 57.0	0.4145	···	3	43.7293
RCC J0223.6-0821	35.9671	−8.36164	0.24	17.2 ± 1.4	35.9666	−8.36037	2.04 ± 0.90	44.4 ± 21.0	0.2287	435 ± 109	7	43.6225
RCC J0223.7-0835	35.977	−8.60424	0.27	32.8 ± 2.3	35.9944	−8.59622	3.51 ± 1.38	102.3 ± 39.3	0.2701	675 ± 142	10	43.7919
RCC J0225.4-0949	36.285	−9.83422	0.18	22.1 ± 1.9	36.2683	−9.82379	3.45 ± 1.16	62.3 ± 18.6	0.1594	516 ± 74	18	43.6489
RCC J0225.6-0623	36.3029	−6.39542	0.2	21.0 ± 1.1	36.3018	−6.3939	5.65 ± 1.77	97.7 ± 32.3	0.2041	452 ± 82	12	43.6016
RCC J0231.6-0452	37.9465	−4.86471	0.21	46.6 ± 2.5	37.9256	−4.87712	9.69 ± 2.44	204.7 ± 49.8	0.1852	425 ± 194	9	44.0886
RCC J0233.0-0942	38.4439	−9.70813	0.25	21.4 ± 2.1	38.426	−9.70045	2.80 ± 1.29	145.6 ± 56.5	0.2646	382 ± 57	19	43.4411
RCC J0849.7-0252	132.292	−2.89579	0.25	13.5 ± 1.6	132.306	−2.87977	1.52 ± 0.85	52.1 ± 23.9	0.2259	516 ± 125	12	43.2838
RCC J0851.3-0416	132.949	−4.26784	0.26	17.0 ± 1.3	132.915	−4.27156	1.33 ± 0.71	28.1 ± 19.0	···	···	···	43.5926
RCC J0852.7-0101	133.048	−1.02552	0.49	40.6 ± 2.3	133.055	−1.02899	4.11 ± 1.46	247.0 ± 113.7	0.4587	415 ± 143	5	44.1486
RCC J0852.5-0534	133.063	−5.57346	0.19	46.9 ± 1.9	133.059	−5.57561	8.99 ± 2.06	130.2 ± 33.3	0.1893	620 ± 156	9	43.9612
RCC J0854.1-0221	133.569	−2.34827	0.36	29.5 ± 2.5	133.562	−2.35264	3.39 ± 1.19	241.3 ± 87.5	0.3679	451 ± 133	9	43.7084
RCC J0856.6-0108	134.114	−1.15371	0.59	14.5 ± 1.7	134.113	−1.14425	3.28 ± 1.17	644.7 ± 250.2	0.623	···	1	43.3342
RCC J0857.1-0343	134.315	−3.7199	0.22	26.2 ± 1.9	134.332	−3.71843	3.03 ± 1.22	21.1 ± 13.5	···	···	···	43.7693
RCC J0858.6-0525	134.668	−5.41993	0.07	30.4 ± 1.6	134.674	−5.42784	4.70 ± 1.45	13.0 ± 4.2	···	···	···	43.5323
RCC J0901.8-0138	135.387	−1.64256	0.3	38.5 ± 0.9	135.391	−1.6481	3.96 ± 1.23	145.8 ± 55.3	0.3163	358 ± 45	17	43.9377
RCC J0901.9-0158	135.424	−1.96503	0.35	14.6 ± 1.1	135.412	−1.98222	1.87 ± 0.87	106.1 ± 47.0	0.3131	387 ± 104	8	43.709
RCC J2214.4-0055	333.571	−0.953427	0.26	18.2 ± 1.2	333.575	−0.9233	4.76 ± 1.82	114.9 ± 47.0	···	···	···	43.6338

(This table is available in its entirety in machine-readable form.)

panel of Figure 16. Column 1 is the cluster ID. The coordinates (R.A. and decl., equinox J2000) of the clusters are given in Columns 2 and 3, respectively. The red sequence redshift and significance (α) are listed in Columns 4 and 5, respectively. The position of the optical center is reported in Columns 6 and 7. Columns 8 and 9 report *ROSAT* X-ray flux and luminosity in units of 10^{-13} erg s^{-1} cm^{-2} and 10^{42} erg s^{-1}, respectively. The spectroscopic redshifts that were also verified visually are given in Column 10. Columns 11 and 12 present the velocity dispersion and the number of spectroscopic member galaxies from Section 3.3, respectively. Based on the derived relation between L_X and L_S, we estimate the $L_X(L_S)$ for 32 RASS clusters. We measured L_S within 1 Mpc from the optical center of clusters (Columns 6 and 7 in Table 6). The estimated cluster L_X using the orthogonal fitting result (in Table 4 with 0.23 and 0.26 dex scatter in X-ray luminosity for low and high redshifts, respectively) is listed in Column 13 of Table 6.

The inferred mass and X-ray luminosity of the *XMM* clusters as a function of redshift are illustrated in Figure 17. We mark 16 *XMM* clusters in common to RASS clusters as squares. This subsample of RASS clusters stems from our targeted follow-up observations of RASS clusters found inside the part of the CFHTLS survey publicly released in T0005 and presents an effective search for massive clusters in the area of 90 deg^2. The two curves in Figure 17 show the detection boundary related to 2×10^{-13} erg cm^{-2} s^{-1} in X-ray flux. This flux is associated with a detection limit over 85% of the survey area. All *XMM* clusters more luminous or massive than these two curves are also identified as RASS clusters using adopted criteria for selection of clusters among RASS sources (see Section 3.5). The mass (and luminosity) detection limit, shown with a curve in Figure 17, also implies that only extreme clusters ($\sim 10^{15}\ M_\odot$) at redshift $\sim$1 are detectable in RASS data.

We added COSMOS X-ray-selected galaxy clusters (Finoguenov et al. 2007; George et al. 2011) to the plots, to show the difference in the cluster sample. At a fixed redshift, the typical mass (and luminosity) of *XMM*-CFHTLS clusters is an order of magnitude more massive (and more luminous) in comparison with a typical group in deep surveys such as COSMOS. For example, at the redshift range of $0.2 \leqslant z \leqslant 0.3$, the median of the M_{200c} of *XMM*-CFHTLS and COSMOS clusters is $1.1 \times 10^{14}\ M_\odot$ and $2.6 \times 10^{13}\ M_\odot$, respectively. This difference in the mean total mass (and luminosity) is even larger between COSMOS and RASS-CFHTLS clusters.

A comparison of the X-ray fluxes from RASS and *XMM* is presented in Figure 18. At low flux levels, the RASS flux estimates are subject to the Malmquist bias, as shown by a model curve. We also report that the mean of distances between the center of RASS and *XMM* X-ray emissions is 0.′6 for 16 clusters in overlap between RASS and *XMM* samples.

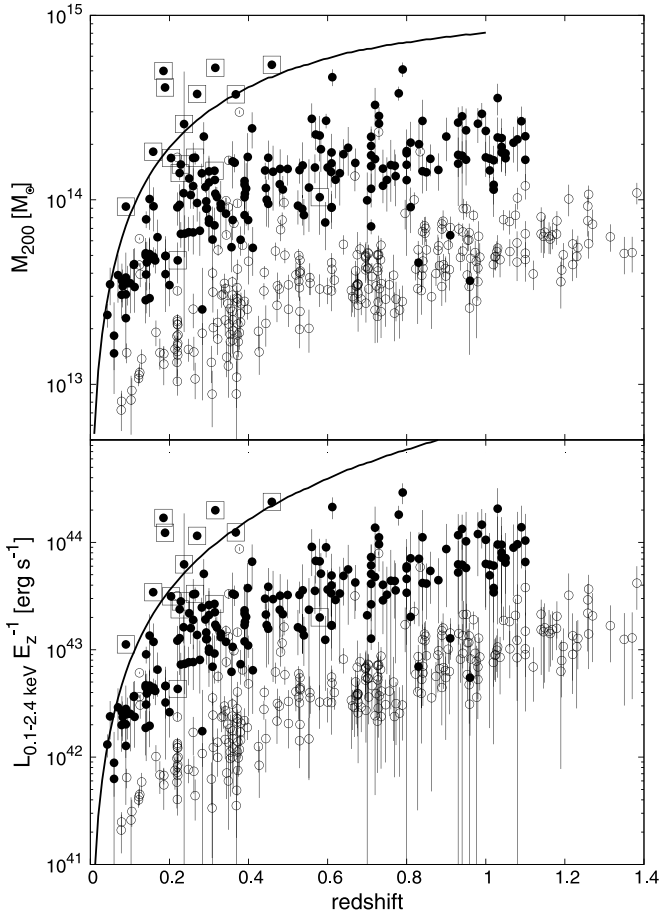

Figure 17. X-ray mass (top) and X-ray luminosity (bottom) as functions of redshift. Black dots and open circles show *XMM*-CFHTLS and COSMOS X-ray-selected galaxy clusters, respectively. The errors are calculated with statistical errors in the X-ray flux measurements. A total of 16 *XMM* clusters in common to RASS clusters are marked as squares. In both panels, the solid curves show the detection limits in luminosity–redshift and mass–redshift spaces corresponding to an X-ray flux limit of 2×10^{-13} erg cm^{-2} s^{-1}.

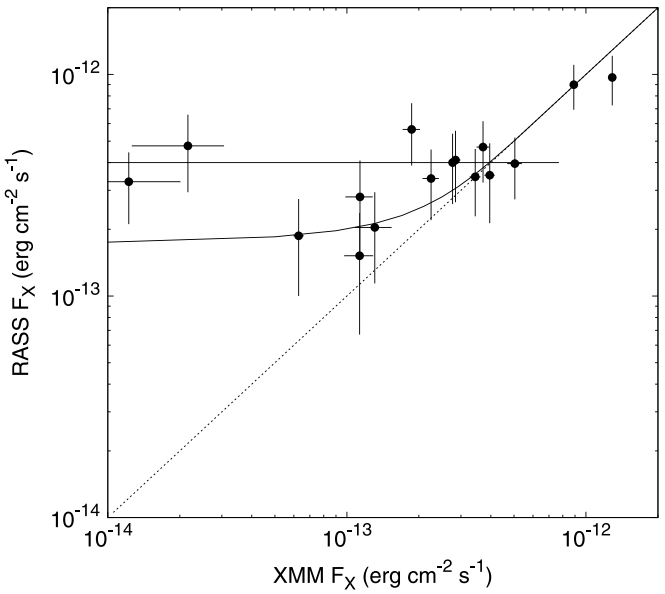

Figure 18. RASS X-ray flux vs. *XMM-Newton* X-ray flux for 16 clusters in overlap between the RASS and *XMM* cluster samples. A solid curve shows the prediction for Malmquist bias in the RASS flux measurement.

5. SUMMARY

We have presented the results of an X-ray search for bright clusters in the CFHTLS fields. In this work we presented the cluster identification in RASS and *XMM* data. We developed a method for identifying clusters at the limits of RASS data, reaching flux levels of 2×10^{-13} erg cm^{-2} s^{-1}, with the help of deep photometric data, such as that of CFHTLS.

We have described a multicolor red sequence finder and calibrated it for CFHTLS $u^*g'r'i'z'$ filters and the redshift below 1.1. The spectroscopic follow-up was done using the Hectospec spectrograph on MMT, with higher priority for clusters with high X-ray flux. To increase the efficiency of spectroscopic follow-up, target galaxies were selected within a range of photometric redshift around the red sequence redshift of clusters. In this work we also used SDSS spectroscopic data in the CFHTLS wide fields. We applied our red sequence finder on RASS and *XMM-Newton* X-ray sources in the W1, W2, and W4 CFHTLS fields. In total, we identified 32 clusters associated with RASS sources and 196 clusters among *XMM* X-ray sources, with a 100% identification rate achieved for the high-significance *XMM* sample. We computed the X-ray luminosity and mass from the X-ray flux and the scaling relations from the literature. In comparison with other *XMM* samples, the clusters in our sample are typically of $\sim 10^{14}\ M_\odot$ masses, while, e.g., COSMOS X-ray-selected groups are of an order of magnitude lower mass. We calculated the velocity dispersions with an iterative gapper method and derive the scaling relation between velocity dispersion and X-ray luminosity of clusters.

We also explored a correlation of integrated optical luminosity and X-ray luminosity. We showed that multicolor red sequence reduces the scatter in relation with X-ray luminosity. This set of optical methods for cluster finding is particularly useful for providing large samples of X-ray-luminous (or massive) clusters (especially for cosmological studies) using shallow X-ray data and wide optical surveys. First, by applying the red sequence finder and maximizing α, we can extract a pure sample of clusters out of a list of X-ray sources. Second, by measuring the optical luminosity of clusters within an appropriate fixed radius, we can estimate the cluster total mass, allowing an efficient separation of high X-ray-luminous (high-mass) clusters for further studies.

We thank Mara Salvato, Daniele Pierini, Claudia Maraston, and Natascha Greisel for help in providing stellar population models. We thank Charles IV Kirkpatrick for the comments on the manuscript.

This work is based on observations obtained with MegaPrime/MegaCam, a joint project of CFHT and CEA/DAPNIA, at the Canada–France–Hawaii Telescope (CFHT), which is operated by the National Research Council (NRC) of Canada, the Institut National des Sciences de l'Univers of the Centre National de la Recherche Scientifique (CNRS) of France, and the University of Hawaii. This research used the facilities of the Canadian Astronomy Data Centre operated by the National Research Council of Canada with the support of the Canadian Space Agency. CFHTLenS data processing was made possible thanks to significant computing support from the NSERC Research Tools and Instruments grant program. This work has been supported by a DLR project 50 OR 1013 to MPE. K.K. acknowledges support from the Magnus Ehrnrooth foundation. A.F. and K.K. wish to acknowledge Finnish Academy award, decision 266918. Funding for SDSS-III has been provided by the Alfred

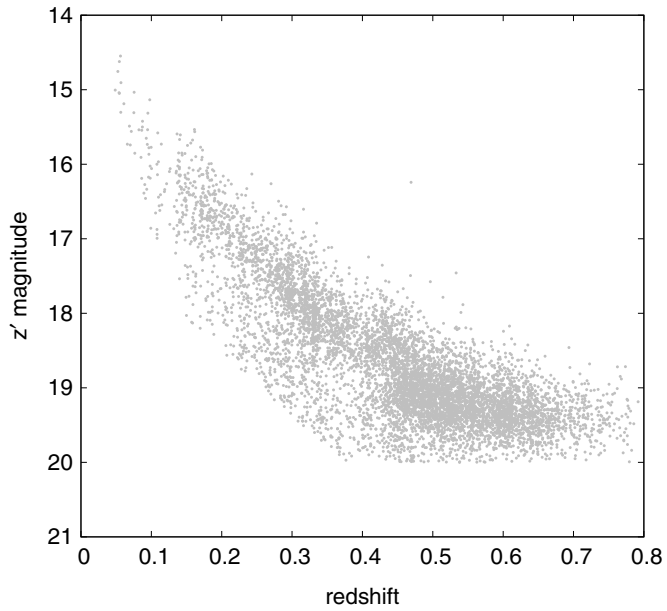

Figure 19. Magnitude–redshift distribution of the ETGs brighter than $z' = 20$ and $m_*(z)$.

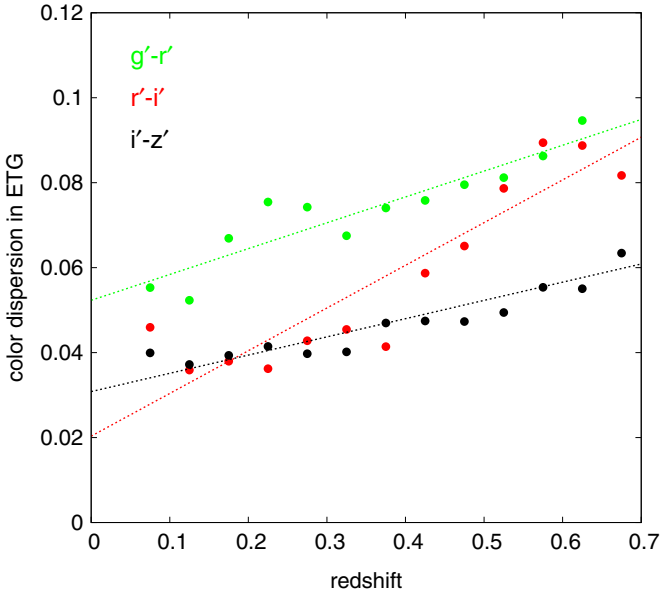

Figure 20. Color evolution of ETGs as a function of redshift. The green, red, and black dots shows the evolution of $g' - r'$, $r' - i'$, and $i' - z'$, respectively, in ETGs with spectroscopic redshift. The dashed lines with the same color codes are linear fits to each galaxy color.

P. Sloan Foundation, the Participating Institutions, the National Science Foundation, and the U.S. Department of Energy Office of Science. The SDSS-III Web site is http://www.sdss3.org/. SDSS-III is managed by the Astrophysical Research Consortium for the Participating Institutions of the SDSS-III Collaboration, including the University of Arizona, the Brazilian Participation Group, Brookhaven National Laboratory, University of Cambridge, Carnegie Mellon University, University of Florida, the French Participation Group, the German Participation Group, Harvard University, the Instituto de Astrofisica de Canarias, the Michigan State/Notre Dame/JINA Participation Group, Johns Hopkins University, Lawrence Berkeley National Laboratory, Max Planck Institute for Astrophysics, Max Planck Institute for Extraterrestrial Physics, New Mexico State University, New York University, Ohio State University, Pennsylvania State University, University of Portsmouth, Princeton University, the Spanish Participation Group, University of Tokyo, University of Utah, Vanderbilt University, University of Virginia, University of Washington, and Yale University.

APPENDIX

COLOR VARIATION OF EARLY-TYPE GALAXIES AS A FUNCTION OF REDSHIFT

In this Appendix we show that intrinsic colors of ETGs have a linear-like evolution through the redshift. In Section 3.1 we derived the color evolution of ETGs using a sample of galaxies with spectroscopic redshift. Here we use a subsample of those galaxies to show that the linear assumption about evolution of intrinsic color dispersion for red sequence galaxies is acceptable. To reduce the effect of error in galaxies observed magnitude, the sample of Section 3.1 was cut by $20 < z'$ and brighter than $m_*(z)$. Figure 19 shows the magnitude and redshift distribution of this sample.

For the faintest galaxies in the sample ($z' = 20$), the typical errors in g', r', i', and z' are $\sim$0.01, 0.008, 0.005, and 0.01. Thus, magnitude errors cannot induce a significant effect on dispersion of colors. Dots in Figure 20 illustrate the color evolution of ETGs as a function of different redshift bins. Dashed lines are linear fitted lines on the color evolution. The mean difference between linear fits and measured color dispersions at a given redshift is 10%, 18%, and, 7% for $g' - r'$, $r' - i'$, and $i' - z'$, respectively. Thus, considering linear evolution for intrinsic color dispersion of ETGs is acceptable, and we generalized this assumption to red sequence galaxies.

REFERENCES

Aihara, H., Allende Prieto, C., An, D., et al. 2011, ApJS, 193, 29
Akritas, M. G., & Bershady, M. A. 1996, ApJ, 470, 706
Allen, S. W., Evrard, A. E., & Mantz, A. B. 2011, ARA&A, 49, 409
Allevato, V., Finoguenov, A., Hasinger, G., et al. 2012, ApJ, 758, 47
Andreon, S. 2012, A&A, 548, A83
Annis, J., Kent, S., Castander, F., et al. 1999, BAAS, 31, 1391
Balogh, M. L., McGee, S. L., Wilman, D. J., et al. 2011, MNRAS, 412, 2303
Bauer, F. E., Alexander, D. M., Brandt, W. N., et al. 2002, AJ, 123, 1163
Baum, W. A. 1959, PASP, 71, 106
Beers, T. C., Flynn, K., & Gebhardt, K. 1990, AJ, 100, 32
Bielby, R. M., Finoguenov, A., Tanaka, M., et al. 2010, A&A, 523, A66
Borgani, S., Rosati, P., Tozzi, P., et al. 2001, ApJ, 561, 13
Bower, R. G., Lucey, J. R., & Ellis, R. S. 1992, MNRAS, 254, 601
Cappelluti, N., Hasinger, G., Brusa, M., et al. 2007, ApJS, 172, 341
Connelly, J. L., Wilman, D. J., Finoguenov, A., et al. 2012, ApJ, 756, 139
Cool, R. J., Howell, S. B., Peña, M., Adamson, A. J., & Thompson, R. R. 2005, PASP, 117, 462
Coupon, J., Ilbert, O., Kilbinger, M., et al. 2009, A&A, 500, 981
Efron, B. 1982, The Jackknife, the Bootstrap (Philadelphia, PA: SIAM) and Other Resampling Plans
Eisenstein, D. J., Annis, J., Gunn, J. E., et al. 2001, AJ, 122, 2267
Erfanianfar, G., Finoguenov, A., Tanaka, M., et al. 2013, ApJ, 765, 117
Erfanianfar, G., Popesso, P., Finoguenov, A., et al. 2014, MNRAS, 445, 2725
Fabricant, D., Fata, R., Roll, J., et al. 2005, PASP, 117, 1411
Finoguenov, A., Connelly, J. L., Parker, L. C., et al. 2009, ApJ, 704, 564
Finoguenov, A., Guzzo, L., Hasinger, G., et al. 2007, ApJS, 172, 182
Finoguenov, A., Streblyanska, A., Hasinger, G., Hashimoto, Y., & Szokoly, G. 2005, AdSpR, 36, 710
Finoguenov, A., Watson, M. G., Tanaka, M., et al. 2010, MNRAS, 403, 2063
George, M. R., Leauthaud, A., Bundy, K., et al. 2011, ApJ, 742, 125
George, M. R., Leauthaud, A., Bundy, K., et al. 2012, ApJ, 757, 2
Giacconi, R., Zirm, A., Wang, J., et al. 2002, ApJS, 139, 369
Giodini, S., Finoguenov, A., Pierini, D., et al. 2012, A&A, 538, A104
Giodini, S., Pierini, D., Finoguenov, A., et al. 2009, ApJ, 703, 982
Gladders, M. D., & Yee, H. K. C. 2000, AJ, 120, 2148

Gozaliasl, G., Finoguenov, A., Khosroshahi, H. G., et al. 2014, A&A, 566, A140
Ilbert, O., Arnouts, S., McCracken, H. J., et al. 2006, A&A, 457, 841
Kettula, K., Giodini, S., van Uitert, E., et al. 2014, arXiv:1410:8769
Koester, B. P., McKay, T. A., Annis, J., et al. 2007, ApJ, 660, 221
Kravtsov, A. V., Vikhlinin, A., & Nagai, D. 2006, ApJ, 650, 128
Leauthaud, A., Finoguenov, A., Kneib, J.-P., et al. 2010, ApJ, 709, 97
Maraston, C., Strömbäck, G., Thomas, D., Wake, D. A., & Nichol, R. C. 2009, MNRAS, 394, L107
Nagai, D., Vikhlinin, A., & Kravtsov, A. V. 2007, ApJ, 655, 98
Nelan, J. E., Smith, R. J., Hudson, M. J., et al. 2005, ApJ, 632, 137
Pacaud, F., Pierre, M., Adami, C., et al. 2007, MNRAS, 382, 1289
Perlmutter, S., Aldering, G., Goldhaber, G., et al. 1999, ApJ, 517, 565
Planck Collaboration, Ade, P. A. R., Aghanim, N., et al. 2014, A&A, 571, A20
Predehl, P., Andritschke, R., Böhringer, H., et al. 2010, Proc. SIPE, 7732, 23
Riess, A. G., Filippenko, A. V., Challis, P., et al. 1998, AJ, 116, 1009
Rosati, P., Borgani, S., & Norman, C. 2002, ARA&A, 40, 539
Rosati, P., della Ceca, R., Norman, C., & Giacconi, R. 1998, ApJL, 492, L21
Rozo, E., & Rykoff, E. S. 2014, ApJ, 783, 80
Ruel, J., Bazin, G., Bayliss, M., et al. 2014, ApJ, 792, 45
Rykoff, E. S., Koester, B. P., Rozo, E., et al. 2012, ApJ, 746, 178
Rykoff, E. S., Rozo, E., Busha, M. T., et al. 2014, ApJ, 785, 104
Silverman, J. D., Kovač, K., Knobel, C., et al. 2009, ApJ, 695, 171
Spergel, D. N., Verde, L., Peiris, H. V., et al. 2003, ApJS, 148, 175
Tanaka, M., Finoguenov, A., Kodama, T., et al. 2008, A&A, 489, 571
Tanaka, M., Finoguenov, A., Lilly, S. J., et al. 2012, PASJ, 64, 22
Vikhlinin, A., Kravtsov, A. V., Burenin, R. A., et al. 2009, ApJ, 692, 1060
Vikhlinin, A., McNamara, B. R., Forman, W., et al. 1998, ApJ, 502, 558
Voges, W., Aschenbach, B., Boller, T., et al. 1999, A&A, 349, 389
Weinberg, D. H., Mortonson, M. J., Eisenstein, D. J., et al. 2013, PhR, 530, 87
Wilman, D. J., Balogh, M. L., Bower, R. G., et al. 2005, MNRAS, 358, 71